ADVANCED FUNCTIONAL MATERIALS
www.afm-journal.de

Synthesis and Electronic Structure of the Fractionally Occupied Double Perovskite $EuTa_2O_6$ with Ordered Europium Vacancies

*Tobias Schwaigert, Ali Barooni, Benjamin Gregory, Paul Malinowski, Anirudh Tenneti, Sonia Hasko, Brenan Palazzolo, Jeffrey W Hodgson, Brendan Faeth, Patrick M. Woodward, Kyle M. Shen, Andrej Singer, Maryam Ghazisaeidi, Salva Salmani-Rezaie, Darrell G. Schlom, and Kaveh Ahadi**

2D electronic states underline a wide range of exotic phenomena and provide potential for electronic devices. The ability to create and control these states often requires physical thinning or highly perfect interfaces. In this work, the "fractional double perovskite" ATa_2O_6 (*A*: Eu^{2+}) is synthesized and characterized, where alternating *A*-site cations and *A*-site vacancies significantly impact the electronic structure, giving rise to a quasi-2D electronic state within a 3D crystal framework. The intrinsic crystal anisotropy of ATa_2O_6 plays a pivotal role, underscoring how targeted structural modifications can facilitate the emergence of novel quantum states. Utilizing single-crystal synthesis via molecular-beam epitaxy, the crystal and electronic structures of ATa_2O_6 are investigated. X-ray diffraction and electron microscopy reveal the layered *A*-site ordering. Synchrotron-based diffraction shows the presence of three epitaxial twin variants of ATa_2O_6 domains, with preferential orientation along out-of-plane direction. Angle-resolved photoemission spectroscopy, along with density functional theory calculations, provide direct insight into the electronic structure, unveiling the potential for engineered confined states within bulk materials. These findings highlight ATa_2O_6 as a platform for studying 2D-like electronic phenomena in a 3D context, paving the way for novel device architectures.

1. Introduction

Structures in which charge carriers flow in two-dimensions are the basis of modern semiconductor technology[1,2] and have facilitated discovery of fundamental states, including integer and fractional quantum Hall[3–6] and exotic superconducting states.[7,8] Such structures are typically realized at the interfaces of two dissimilar materials or through physical dimensional reduction. The realization of interfacial 2D electronic states and quantum confinement requires engineered band alignment and sophisticated synthesis techniques. The physical dimensional reduction approach is limited to materials systems where out-of-plane bonding is weak, i.e., van der Waals materials. Realization of intrinsic 2D electronic states and transport in 3D crystals are highly desirable.

Transition metal complex oxides exhibit a wide variety of orders and instabilities that are highly tunable.[9–14] 2D electron

T. Schwaigert, A. Tenneti, J. W Hodgson, A. Singer, D. G. Schlom
Department of Materials Science and Engineering
Cornell University
Ithaca, NY 14853, USA

A. Barooni, M. Ghazisaeidi, S. Salmani-Rezaie, K. Ahadi
Department of Materials Science and Engineering
The Ohio State University
Columbus, OH 43210, USA
E-mail: ahadi.4@osu.edu

The ORCID identification number(s) for the author(s) of this article can be found under https://doi.org/10.1002/adfm.202513656

DOI: 10.1002/adfm.202513656

B. Gregory, P. Malinowski, K. M. Shen
Department of Physics
Cornell University
Ithaca, NY 14853, USA

B. Gregory, K. M. Shen
Laboratory of Atomic and Solid State Physics
Department of Physics
Cornell University
Ithaca, NY, USA

S. Hasko, B. Palazzolo, B. Faeth
Platform for the Accelerated Realization, Analysis, and Discovery of Interface Materials (PARADIM)
Cornell University
Ithaca, NY 14853, USA

S. Hasko
Department of Chemical and Biological Engineering
Princeton University
Princeton, NJ, USA

systems in oxides, commonly realized at the interface of two insulating oxide layers, could exhibit entirely new properties and phenomena.[15,16] For example, exotic emergent phenomena and functional properties, including tunable superconductivity,[17,18] fractional quantum hall,[19] emergent magnetism,[20,21] metal-to-insulator transition,[22] efficient spin-to-charge interconversion,[23,24] and tunable Rashba splitting[25] and Berry curvatures[26,27] have been reported at these interfaces.

Oxide materials allow for control and high degrees of tunability of electronic structure with crystal symmetry and ordering. Here, we realize and control 2D electronic states by *crystal anisotropy* rather than conventional interfacial engineering or physical dimensional reduction. By distorting the bonding network within the well-known perovskite structure, it is possible to create quasi-2D electronic states, in which the electronic wave function is intrinsically confined within the distinct layers stacked along the crystalline *c*-axis. In the perovskite-derived $EuTa_2O_6$, structural anisotropy due to *A*-site ordering is predicted to create a 2D electronic state that hosts topologically non-trivial spin textures.[28] This makes $EuTa_2O_6$ an ideal candidate for intrinsic confinement of charge carriers, offering a novel platform where quantum transport properties can be manipulated through structural design rather than traditional interface engineering or exfoliation.

The physical properties and emergent phenomena in transition metal oxides are highly tunable with lattice distortions as the crystal structure deviates from the perovskite aristotype.[29,30] Here, we focus on cation substitution and ordering of vacancies. While the *B*-site ordering, including vacancy ordering[31] and its effect on physical properties have been extensively studied in perovskites,[32–34] *A*-site ordering and its effect on physical properties have only been explored recently.[35] *A*-site layered ordering could be an efficient tuning knob in complex oxides. For example, the *A*-site ordered double perovskites $BaSmMn_2O_6$ and $BaLaMn_2O_6$ exhibit significantly different spatial arrangements of charge and orbital ordering of the Mn^{3+} and Mn^{4+} ions as well as charge-ordering phase transition temperatures (T_{CO}), compared to their disordered counterparts ($Ba_{1/2}RE_{1/3}MnO_3$).[36,37] In contrast to conventional (double) perovskites, *fractional perovskites* exhibit non-standard *A*-site stoichiometries due to the substitution of the monovalent *A*-site cation in $A^+B^{5+}O_3{}^{2-}$ with divalent (e.g., Eu^{2+} or Sr^{2+}) or trivalent (e.g., Sm^{3+} or Gd^{3+}) cations. To preserve charge neutrality, half (A^{2+}) or two-thirds (A^{3+}) of the *A*-site positions must remain vacant. The *A*-site cations and vacancies can adopt layered ordering. In analogy to conventional perovskites—where cation ordering results in a doubled formula unit—these phases may appropriately be referred to as *fractional double perovskites*, reflecting both their fractional *A*-site occupancy and structural ordering.

In addition to chemical control, epitaxial strain serves as a powerful tuning parameter that can significantly alter lattice symmetry, affect phase stability, and reshape the energy landscape—thereby influencing ordering tendencies within these systems. Notably, strain has been shown to induce ferroelectric behavior and modify octahedral rotation patterns in perovskite systems, demonstrating its effectiveness in controlling symmetry and functional properties.[38–40] Strain-driven modifications to the energy landscape may further influence ordering behavior, including the possibility of relaxation via in-plane ordering or local disorder. Prior studies have demonstrated that intentionally mismatched substrates can be used not only to affect the orientation of the epitaxial domains, but also to direct the ordering of oxygen vacancies in ways to reduce strain.[41,42]

In this work, we synthesize partially ordered ATa_2O_6 by molecular-beam epitaxy (MBE), in which layered ordering of *A*-cations and *A*-site vacancies modifies the electronic landscape, favoring 2D electronic states. While this manuscript focuses on *A*: Eu^{2+}, other fractional double perovskites, such as *A*: Sr^{2+} may also be realized. Preliminary growth and characterization of *A*: Sr^{2+} is included in the Supporting Information. Here, we achieve ATa_2O_6 epitaxial films, consisting of layered ordering of *A*-cations and *A*-site vacancies along the *c*-axis. This ordering results in a 2D electronic structure, consistent with density functional theory (DFT) predictions and angle-resolved photoemission spectroscopy (ARPES) observations.

2. Results and Discussion

2.1. Structural Investigation by X-Ray Diffraction

In $EuTa_2O_6$ half of the *A*-site cations are vacant compared to a conventional double-perovskite structure, $AA'B_2O_6$. Two idealized ways in which the missing europium could be accommodated are shown in **Figure 1**a,b. In Figure 1a the *AO* layers of the double perovskite structure alternate with full and empty EuO layers along the crystallographic *c*-axis. In Figure 1b the Eu-sites are randomly filled with 50% occupancy. In the former case, the unit cell of the $EuTa_2O_6$ crystal structure is composed of one $EuTa_2O_6$ formula unit along the crystallographic *c*-axis, alternating between an unoccupied *A*-site and a fully occupied *A*-site. The lattice parameters for such a hypothetical ordered compound, calculated using first principles, are $a = b = 3.926$ Å and $c = 7.929$ Å, which are larger than those measured experimentally on samples prepared by conventional solid-state synthesis.[43] If Eu^{3+} is formed, a partially occupied *A*-site layer is required in place of the fully occupied *A*-site to satisfy charge neutrality. While RTa_3O_9 (R^{3+} = rare earth, including Eu) has been synthesized by solid-state reaction methods,[44,45] little is known about the Eu^{2+} equivalent $EuTa_2O_6$. Nagata, Morita, and Ebisu[44] investigated magnetic properties for various R^{3+} (R = rare earth) in a 12-fold cubic coordination environment. They, however, did not investigate the ordering in various RTa_3O_9 compounds. Wallwork et al.[45]

B. Palazzolo
Department of Physics and Astronomy
Clemson University
Clemson, SC 29631, USA
P. M. Woodward
Department of Chemistry
The Ohio State University
Columbus, OH 43210, USA
D. G. Schlom
Kavli Institute at Cornell for Nanoscale Science
Ithaca, NY 14853, USA
D. G. Schlom
Leibniz-Institut für Kristallzüchtung
Max-Born-Straße 2, 12489 Berlin, Germany

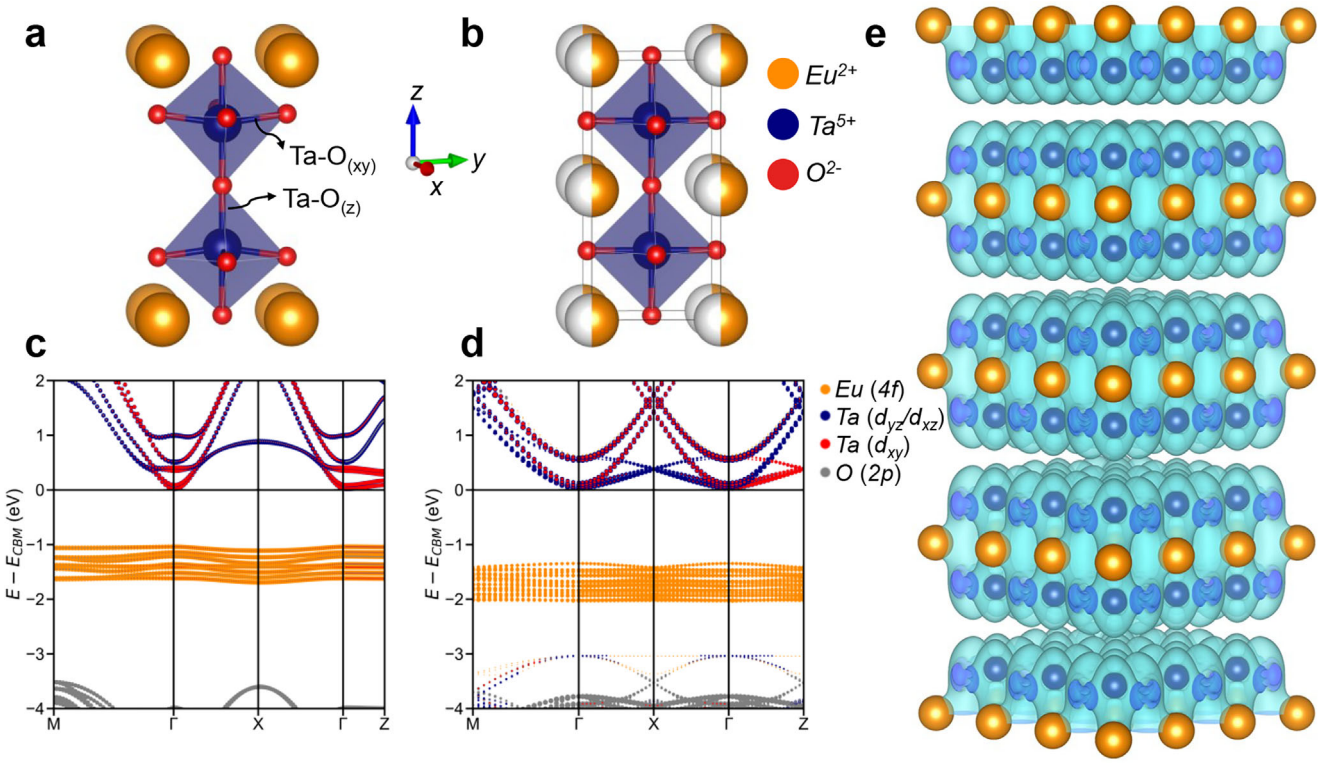

Figure 1. a,b) *A*-site cation ordering schemes in fractional double perovskites AB_2O_6. Illustrations were prepared with VESTA.[20] Orbital-projected band structure of c) ordered $EuTa_2O_6$ and d) randomly occupied $Eu_{0.5}TaO_3$ calculated by DFT. e) Calculated spatial charge distribution of $EuTa_2O_6$ for Fermi level set to 0.1 eV above the conduction band minimum.

investigated octahedral tilting patterns that emerge while varying the R^{3+} cations, referring to their compounds as $R_{1/3}TaO_3$ rather than RTa_3O_9, without quantifying ordering. For *A*-site ordered double perovskites, the preferred hettotype is a layered plane type. This is stabilized by *A*-site vacancies coupled with second-order Jahn–Teller distortions (SOJT) of the *B*-site cations and the presence of highly charged d^0 cations.[35] DFT calculations give insight into the magnitude of SOJT distortions. Here, the apical Ta—$O_{(z)}$ (Å) bond length toward the vacant layer has shortened to 1.906 Å, while the Ta—$O_{(z)}$ (Å) bond length toward the EuO layer has elongated to 2.054 Å from the symmetrical apical bond distance of 1.980 Å. Figure 1b shows the crystal structure where the *A*-site cation and the vacancies are randomly distributed, resulting in a net occupancy of 0.5 in the *A*-site layers. $EuTa_2O_6$ could also form within the limits depicted in Figure 1 (i.e., partially ordered).

Figure 1c depicts the calculated band structure of $EuTa_2O_6$. The tantalum SOJT distortion breaks the degeneracy of Ta t_{2g}-derived conduction band and pushes the d_{xy} down in energy. The d_{xy} orbitals have suppressed out-of-plane hopping and, as a result, the conduction band edge exhibits dispersive behavior along the Γ→X and Γ→M directions while appearing flat along Γ→Z. The Fermi surface near the conduction band edge exhibits a tube-like structure in ordered $EuTa_2O_6$ due to Ta^{5+} d_{xy} orbital character (Figure S1, Supporting Information). Figure 1e exhibits the spatial distribution of charge density with the Fermi level set to 0.1 eV just above the minimum energy of the lowest energy conduction band. Figure 1d highlights the impact of *A*-site ordering on the electronic structure. The magnitude of SOJT is governed by the degree of ordering. Randomly distributed Eu^{2+} impacts the Ta—O bond length symmetrically. As a result, the Ta t_{2g}-derived conduction band is dispersive along Γ→X, Γ→M, and Γ→Z, suggesting a 3D charge distribution. The quasi-2D nature of $EuTa_2O_6$ is reduced as the charge transfer between Eu^{2+} and O^{2-} becomes increasingly degenerate due to the gradual loss of SOJT, which is caused by the random distribution of europium atoms.

In conventional layered oxides such as high-*T*c cuprates and Ruddlesden–Popper (RP) phases, 2D electron confinement is primarily governed by the CuO_2 planes, where the electronic structure is dominated by strongly hybridized Cu $3d_{x^2-y^2}$ and O 2*p* orbitals.[46] These active planes are separated by charge reservoir layers, which act as electronic barriers and enhance the 2D confinement by minimizing interlayer coupling. In contrast, $SrRu_2O_4$ —a prototypical RP ruthenate—exhibits a distinct electronic configuration governed by the Ru 4*d* t_{2g} manifold, including d_{xy}, d_{xz}, and d_{yz} orbitals.[47] Here, due to the more spatially extended nature of 4*d* orbitals, compared to 3*d* orbitals, the degree of electron correlation and confinement is inherently weaker, leading to more 3D electronic behavior in some orbitals despite structural layering. Resistivity versus temperature reveals a changing ratio with a maximum of 200 between the *a*-*b*-plane and *c*-plane ≈130 K.[48]

Remarkably, in the 5*d* system $EuTa_2O_6$, the degree of 2D confinement can be manipulated through vacancy ordering without

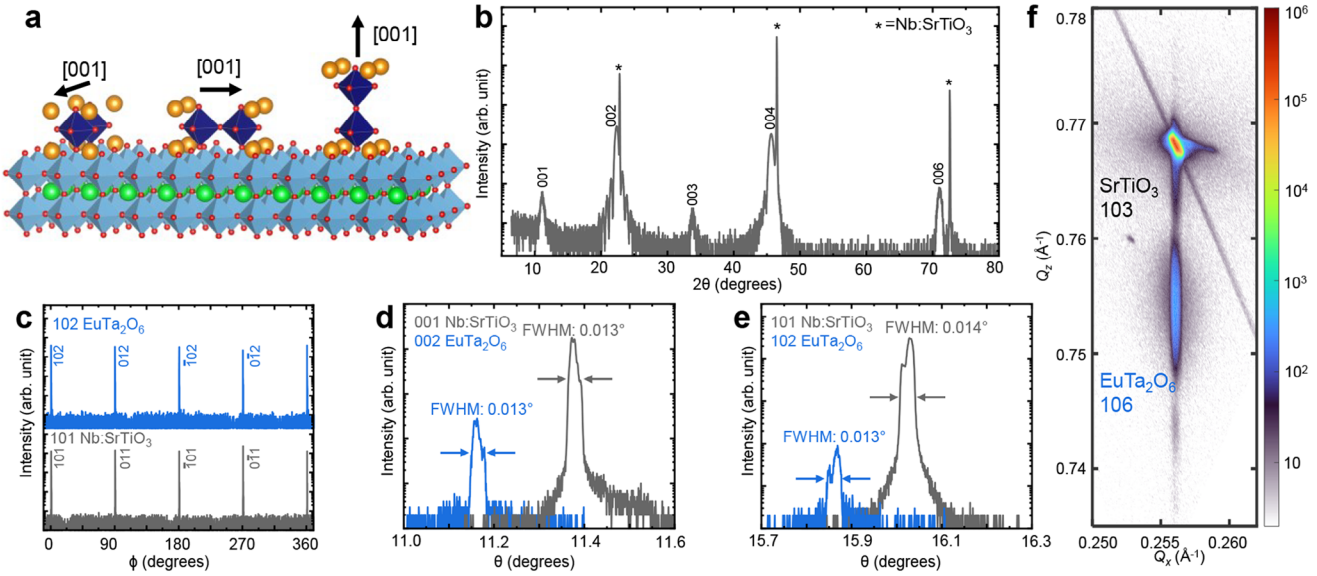

Figure 2. X-ray diffraction of a 16.3 nm thick film of $EuTa_2O_6$ grown on (001) Nb:$SrTiO_3$: a) Proposed epitaxial orientation of $EuTa_2O_6$ on $SrTiO_3$ (001) illustrated with VESTA.[20] b) Symmetrical θ-2θ scan showing only 00ℓ peaks of $EuTa_2O_6$. Laue oscillations indicate a well-defined film thickness, caused by an abrupt interface between film and substrate. c) ϕ-scans around the 103-type substrate and 106-type film reflections. d) Overlaid rocking curves of 001 $SrTiO_3$ and 002 $EuTa_2O_6$ reflections, showing comparable FWHMs, indicating low out-of-plane mosaicity ($\Delta\omega \approx 0.013°$). e) Overlaid rocking curves of 101 $SrTiO_3$ and 102 $EuTa_2O_6$ reflections, showing comparable FWHMs ($\Delta\omega \approx 0.013°$), indicating that the in-plane mosaicity is also low. f) Reciprocal space map (RSM) around the 103 substrate and 106 film reflection. The RSM results confirm that the film is commensurately strained to the substrate.

significantly altering the composition or lattice constants. The 5*d* orbitals of tantalum are even more delocalized than 4*d*, leading to reduced electronic correlations. The intentional breaking of the t_{2g} degeneracy via ordered vacancies offers a unique avenue to tune orbital anisotropy and modulate the dimensionality of electronic transport. This tunability enables exploration of confinement regimes analogous to those found in conventional cuprates, but within a chemically and structurally stable framework.

Since the proposed $EuTa_2O_6$ out-of-plane lattice constant is $c/2 = 3.964$ Å $> a = b = 3.925$ Å; $SrTiO_3$ ($a = 3.905$ Å) was selected as the substrate for thin film growth. $EuTa_2O_6$ on $SrTiO_3$ exhibits a lattice mismatch of −0.5% in the out-of-plane orientation, where the *c*-axis of $EuTa_2O_6$ is perpendicular to the substrate surface. In contrast, if $EuTa_2O_6$ is grown with the *c*-axis lying in-plane – i.e., parallel to the substrate surface, along either the *a*- or *b*-axis of the $SrTiO_3$ substrate – the mismatch increases to −1.5%.

Intentionally mismatched substrates have been shown to promote the orientated incorporation of planes of oxygen vacancies.[41,42] Competition between different epitaxial orientations of the $EuTa_2O_6$ could lead to additional relaxation mechanisms. To promote the epitaxial growth of $EuTa_2O_6$ with layered ordering of Eu^{2+} and vacancies along out-of-plane direction (*c*-axis oriented $EuTa_2O_6$), a substrate imparting a low compressive strain is helpful, as higher strain levels may lead to other polymorphs.[49]

Figure 2a illustrates the potential epitaxial orientations of $EuTa_2O_6$ unit cells on the substrate surface. Three twin variants are possible with good lattice match: the *c*-axis of $EuTa_2O_6$ could lie along one of the <100> in-plane directions of the $SrTiO_3$ (001) substrate or along the out-of-plane [001] direction. Stabilizing a particular Eu/vacancy arrangement depends on synthesis conditions, e.g., temperature, pressure, and stoichiometry. The impact of the growth conditions on the layered ordering of europium/vacancy planes have been explored. An extended description can be found in Section S2 and Figures S2–S6 (Supporting Information). The most critical ordering tuning knob is the holding time at the end of each layer. Increasing this time enhances the degree of ordering while maintaining the stoichiometry. Figure 2b exhibits the symmetrical θ-2θ scan for a 16.3 nm thick film of $EuTa_2O_6$ grown on Nb:$SrTiO_3$ (001) under growth conditions that are optimized for out-of-plane layered ordering. The film thickness is calculated using the Laue fringes and corroborated with x-ray reflectivity and cross-sectional HAADF-STEM. The Bragg reflections $hk\ell$ in the θ-2θ scan (Figure 2b–f) are indexed based on ordered doubled unit cell with ≈8 Å length along the *c*-axis. The θ-2θ scan shows only 00ℓ reflections, confirming that the film is single phase and oriented with its *c*-axis perpendicular on the plane of the substrate. No secondary phases or additional epitaxial orientations are detected in asymmetric ϕ-scans of the {103} family of planes of the $SrTiO_3$ substrate and the {106} family of planes of the $EuTa_2O_6$ thin film (Figure 2c). The rotational symmetry of the film and substrate are identical, indicating the absence of twins that are rotated in-plane. The rocking curve full width at half maximum (FWHM) of the $EuTa_2O_6$ film is comparable to the $SrTiO_3$ substrate (both ≈47 arc sec, respectively) for the 001 $SrTiO_3$ and 002 $EuTa_2O_6$ peak, and 50 arc sec for the 103 $SrTiO_3$ substrate and 47 arc sec for the 106 $EuTa_2O_6$ film peak. X-ray reciprocal space mapping (RSM) around the $SrTiO_3$ 103 and $EuTa_2O_6$ 106 reflections confirm that the film is coherently strained to the substrate (Figure 2f). These XRD scans indicate that there are negligible domains with their crystallographic *c*-axis oriented parallel to the substrate. Reflection high-energy electron diffraction (RHEED) indicates the presence of surface reconstructions on $EuTa_2O_6$ (Figure S7,

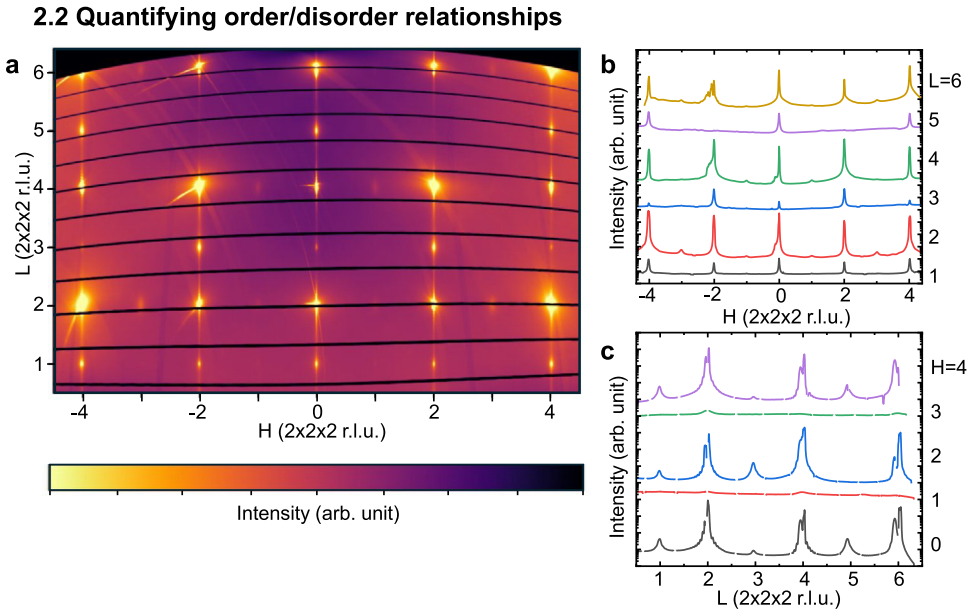

Figure 3. Hard x-ray reciprocal space mapping of a 16.3 nm thick film of $EuTa_2O_6$ on (001) Nb:$SrTiO_3$: a) map of reciprocal space at 300 K, at K = 2 in the (2 × 2 × 2) unit cell notation. b) Line profile along the H2L (H=1-6) directions. c) Line profile along the H2L (L=1–4) directions.

Supporting Information). Atomic force microscopy (AFM) images at different magnifications are shown in Figure S8 (Supporting Information). Atomic steps from the <0.05° substrate off-cut angle are visible. The root-mean-square (rms) roughness for the $EuTa_2O_6$ on $SrTiO_3$ is ≈ 1 nm, measured by taking a 10 μm^2 area as a reference.

The out-of-plane lattice spacing of this commensurately strained film on $SrTiO_3$ is 7.957 ± 0.01 Å. First-principles calculations predict this length to be 7.960 Å for films coherently strained to $SrTiO_3$. The even-even-odd $hk\ell$ reflections 001 and 003 are indicative of the ordering of occupied and unoccupied *A*-site layers (these correspond to half-integer peaks of the pseudo cubic perovskite unit cell, $Eu_{0.5}TaO_3$), while the 002, 004, and 006 peaks represent fundamental perovskite reflections.

2.2. Quantifying Order/Disorder Relationships

We note that, in addition to the domains with *c*-axis oriented along the out-of-plane, other types of structural ordering—such as columnar and rock-salt ordering—as well as distortions like octahedral tilting and twisting remain conceivable. For the close structural relative $Sr_{0.5}TaO_3$, octahedral tilting has been previously reported.[50] In our case, weak reflections that can be attributed to octahedral tilting were also observed in RSM sections. The presence of domains and the coexistence of ordered and disordered regions, however, complicate unambiguous structural assignment (Figures S10–S12, Supporting Information). Table S1 (Supporting Information) summarizes the potential space groups compatible with the parent crystal structure of $EuTa_2O_6$. The analysis was carried out using ISODISPLACE package.[51]

Figure 3a shows an RSM section of the same 16.3 nm $EuTa_2O_6$ film on Nb:$SrTiO_3$. Out-of-plane even-even-odd reflections can be readily observed, while reflections that indicate in-plane ordering are faint in the extracted line profiles (Figure 3b,c). The ratio between out-of-plane and in-plane domains can be estimated by comparing the relative intensity of the 124 and 421 peaks. Measured ratio of ≈10, suggests that out-of-plane domains are favorable by at least an order of magnitude. The large-scale absence of other competing orders can be explained by simple crystal chemistry arguments. Difference in charge and ionic size are generally accepted as factors that stabilize order.[35,52] The layered ordering results in three different bonding environments, namely the apical oxygen in the europium layer (i), equatorial oxygen in the tantalum layer (ii) and apical oxygen in the europium vacant layer (iii). This leads to three distinct charged layers: $(EuO)^0$, $(TaO_2)^{1+}$, and Eu-Vacancy $(O)^{2-}$. The interface charges and subsequent polar catastrophe caused by the out-of-plane ordering can be mitigated by intermixing which has been observed in similar systems.[53,54] In contrast, when the $EuTa_2O_6$ *c*-axis is grown with the *c*-axis lying in-plane – i.e., parallel to the substrate surface, the three distinct charged layers interface the neutral SrO or TiO_2 layers, giving rise to various polar catastrophes, which are energetically unfavorable.

We estimated the total out-of-plane ordering by comparing the relative intensities of the even-even-odd 00ℓ and even-even-even 00ℓ diffraction peaks. Structure factor calculations were performed using the dedicated software package (Peak-Ordering Measurement for Multi-Element Systems (POMMES), available on-line[55]). To validate our model, we employed RIETAN-FP,[56] accessed through VESTA,[57] as described in the supporting Information. Figure S12 (Supporting Information) demonstrates the capability of POMMES to assess diffraction intensities via structure factor calculations, while varying the *A*-site order in comparison to existing packages like VESTA and RIETAN-FP. Figure S13 (Supporting Information) highlights the effect of europium occupancy on the theoretical intensity ratios between different diffraction peaks. Conceptually, the intensity of even-even-odd

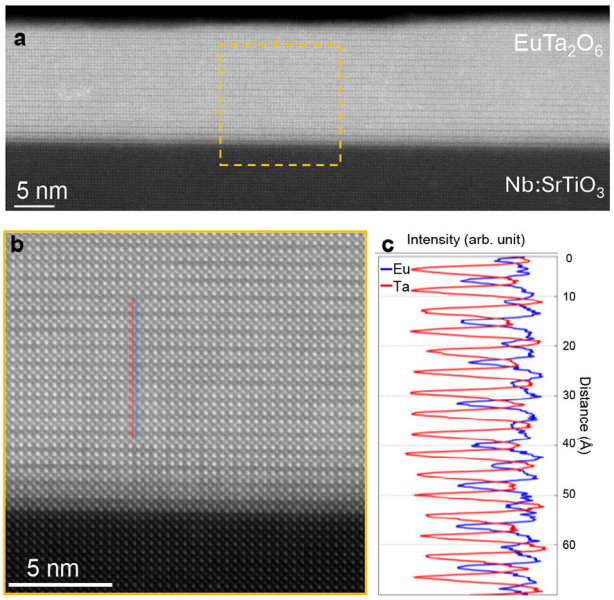

Figure 4. a) Cross-sectional HAADF-STEM images of the same 16.3 nm thick film of $EuTa_2O_6$ grown on $SrTiO_3$ (001) analyzed in Figure 2. b) Higher magnification HAADF-STEM image of the $EuTa_2O_6/SrTiO_3$ interface showing the partially intermixed bilayer. c) Line scan profile along europium and tantalum positions extracted from the marked areas of the HAADF-STEM images (b).

reflections vanishes as the fully disordered structure, $Eu_{0.5}TaO_3$, is approached. In contrast, the maximum intensity is reached when the fully ordered structure is achieved. Here, the ordering parameter $\sigma = (N_F - N_E)/N_t$, is defined as the difference of N_F (number of *A*-site cations in the nominally filled layer) and N_E (number of *A*-site cations in the nominally empty layer), divided by the total number of *A*-site cations N_t. We assume that the total number of *A*-site cations equals the number of *A*-site cations in a stoichiometric fractional double perovskite, AB_2O_6. The Eu occupancy varies from 1 to 0.5 in nominally filled layer while calculating the intensity ratios between even 00ℓ and odd 00ℓ peaks, and was compared to the measured intensity ratios of our grown samples. The ratios are computed between all accessible combinations of fundamental peaks (002, 004, and 006) and ordering peaks (001 and 003). The ordering peak 005 was calculated to have a much smaller intensity and is not experimentally observed. σ is estimated to be 0.32 ± 0.07, implying that the Eu-site occupancy alternates between $64\% \pm 7\%$ in the nominal EuO layer and $36\% \pm 7\%$ for the nominal vacant plane sample shown throughout Figures 2–5. Those values are slightly lower compared to HAADF-STEM quantitative analysis, which acts as a local probe, whereas the X-ray diffraction-based analysis can be seen as a global probe.

2.3. Structural Investigation by HAADF-STEM

High-angle annular dark-field scanning transmission electron microscopy (HAADF-STEM) was employed to investigate the atomic-scale structure of the $EuTa_2O_6$ thin films. **Figure 4a** presents a cross-sectional HAADF-STEM image along the $SrTiO_3$ [100] zone axis, clearly illustrating a coherent and epitaxial interface between the $EuTa_2O_6$ film and the $SrTiO_3$ substrate. $EuTa_2O_6$ exhibits an intrinsic polar stacking along its *c*-axis direction. At the interface with $SrTiO_3$, approximately two atomic layers show intermixed metal ions, which likely mitigate the electrostatic instability (polar discontinuity) inherent to the interface, thereby stabilizing epitaxial growth. The film surface is smooth and well-defined without notable interfacial roughness. A periodic variation in europium column intensity is clearly observed in the intensity line scan profile (Figure 4c). Specifically, europium column intensities (blue curve in Figure 4c) alternate periodically between high and low values, indicating layers with greater and lesser europium occupancies, respectively. In contrast, tantalum columns (red curve in Figure 4c) exhibit relatively constant intensity. Quantitative analysis indicates a europium occupancy of ≈66% ± 12% in nominally occupied layers and ≈34% ± 12% in nominally vacant layers (Figure S14, Supporting Information).

Some localized regions exhibit twin formation with the *c*-axis along an in-plane direction, while other regions exhibit reduced ordering, attributable primarily to random europium occupancy variations rather than alternative structural configurations. Electron diffraction patterns (Figure S15, Supporting Information) confirm this interpretation, as superlattice reflections associated with out-of-plane ordering vanish in regions of reduced europium ordering without the appearance of in-plane ordering reflections.

2.4. Electronic Structure by ARPES

Figure 5 shows the electronic structure of $EuTa_2O_6$ measured by ARPES and core-level XPS spectroscopy. Following growth, the sample was transferred under ultra-high vacuum from the MBE into the ARPES chamber. While previous theoretical work has shown that both $EuTa_3O_9$ and $EuTa_2O_6$ feature a band structure with characteristically similar features,[28] we focus on $EuTa_2O_6$ with europium in the 2+ oxidation state, as this compound has not been stabilized previously.

Core level peaks of europium 3*d* and tantalum 4*f* of the same 16.3 nm thick film (as characterized in Figures 2–4) are shown in Figure 5a. The Eu^{2+} $3d_{5/2}$ and Eu^{2+} $3d_{3/2}$ spin-orbit components are the main features observed, in agreement with europium in the 2+ oxidation state.[58,59] Two additional peaks with lower intensity at 1134 and 1163 eV, are attributed to satellite peaks or weak contributions from Eu^{3+}.[59] The Ta^{5+} $4f_{7/2}$ and Ta^{5+} $4f_{5/2}$ peaks are at 26.25 and 28.00 eV, respectively, and are attributed to a chemical shift caused by changes to oxygen to tantalum ratios.[60,61]

Figure 5c exhibits the band structure density of states calculated by DFT. Further details of the electronic band structure are revealed by VUV photoemission measurements (Figure 5d–g). For the measurements, we assume an in-plane Brillouin zone boundary matching that of the underlying Nb:$SrTiO_3$ substrate (black outline, Figure 5e,f). In qualitative agreement with expectations from previous DFT calculations,[28] the measured valence band structure consists of a detailed O 2*p* manifold between 4 and 9 eV in binding energy, and fainter, nearly dispersion-free Eu 4*f* bands at lower binding energies within the bandgap. All spectral weight vanishes near the Fermi level (Figure 5b, inset), indicating that the conduction band minimum is sufficiently above

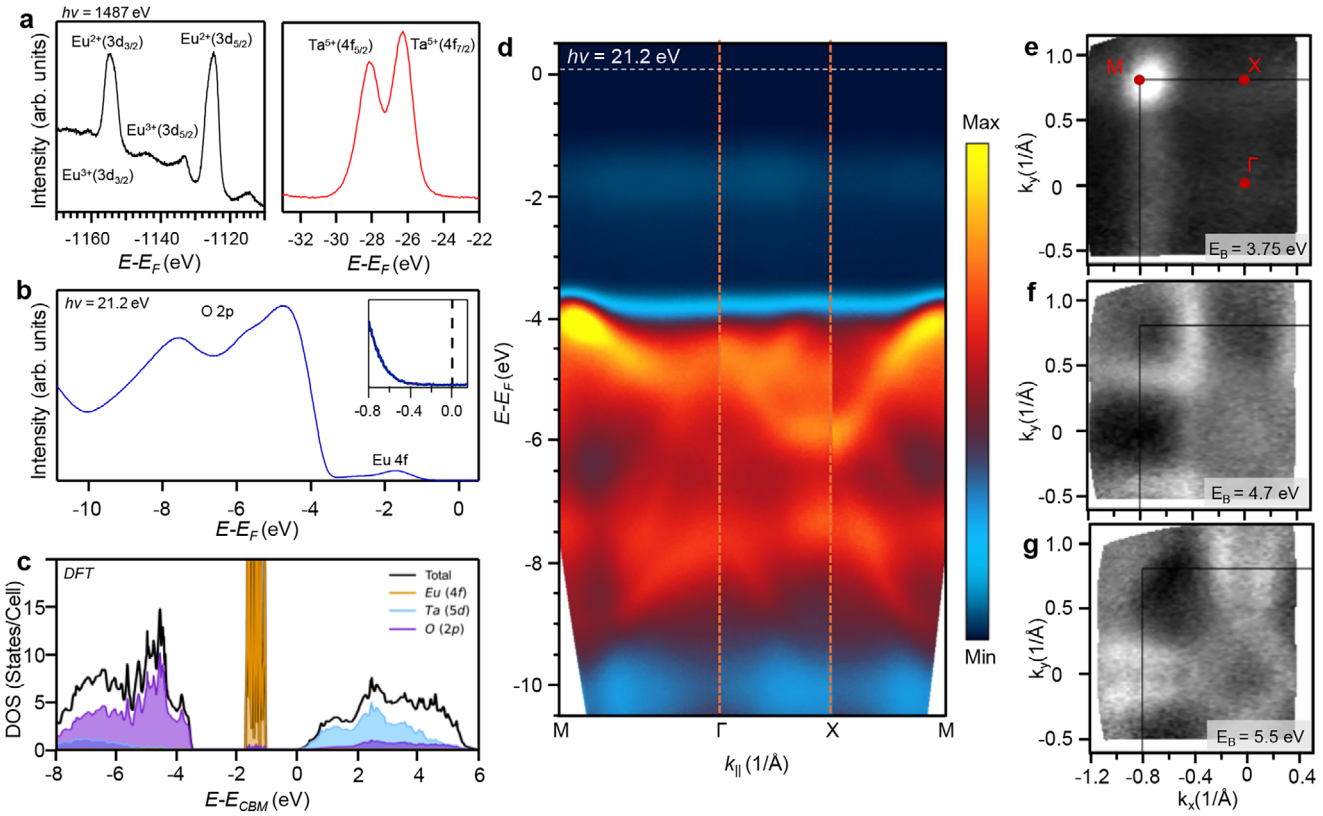

Figure 5. a) High-resolution XPS spectrum of the Eu 3*d* and Ta 4*f* regions, respectively, for a 16.3 nm thick film of $EuTa_2O_6$ grown on Nb:$SrTiO_3$. b) Angle-integrated UV valence-band spectra showing O 2*p* and Eu 4*f* states. c) First-principles calculations of the density of states (DOS) of $EuTa_2O_6$. d In situ angle-resolved valence band structure, measured with an incident photon energy of 21.2 eV. e–g) Selected iso-energy momentum-maps throughout the dispersive O 2*p* manifold, integrated over ± 20 meV of the listed binding energy. Black lines indicate the nominal Brillouin zone boundary for the underlying $SrTiO_3$ substrate. All measurements were performed in situ without exposure to atmosphere and with the film held at room temperature.

the Fermi level to preclude the observation of Ta *d* orbitals. Here, the charge carriers are due to oxygen vacancies. The formation of Eu^{3+}, however, could play a role in the creation of defect centers that cause charge compensation. This was previously studied in $La_{2/3}TiO_3$ where charge neutrality reduces some of the Ti^{4+} ions to Ti^{3+}.[62]

As mentioned earlier, we also have synthesized ordered $SrTa_2O_6$ films epitaxially. $SrTa_2O_6$ films exhibit superior structural quality comparable with $EuTa_2O_6$, evident from XRD and AFM experiments (Figures S16 and S17, Supporting Information). Interestingly, line profiles extracted from AFM micrographs reveal atomic step height, corresponding to the ordered polymorph (d = 7.4 Å). Single oxidation state of strontium (Sr^{2+}) allows efficient electron doping of $SrTa_2O_6$ with oxygen vacancies, which enables clear illustration of the Ta *d* bands and corresponding Fermi surface using ARPES. Figure S18a–e (Supporting Information) exhibits the dispersion of the conduction band derived from d_{xy} orbital at different photon energies ranging from 16.85 to 26.9 eV. Figure S18g (Supporting Information) compares the angle-integrated EDC's between $EuTa_2O_6$ and $SrTa_2O_6$. A clear shift in the O *2p* states to higher binding energy in $SrTa_2O_6$ compared to $EuTa_2O_6$ coincides with the appearance of spectral weight (the 2D Ta *d* bands) below the Fermi level. Figure S19 (Supporting Information) exhibits the corresponding Fermi surface using various photon energies, i.e., different K_Z cuts of the Fermi surface, confirming that while the conduction band is dispersive in-plane, it remains primarily non-dispersive along the out-of-plane direction. The lack of out-of-plane dispersion is consistent with DFT (Figure S1, Supporting Information) and confirms the 2D character of the conduction band. Furthermore, the circular Fermi surface in K_x-K_y projection is consistent with the predicted d_{xy}-derived conduction band edge.

Next, we discuss the robustness of 2D electronic states in partially ordered films. Figure S20 (Supporting Information) exhibits the DFT calculation for ideal and partial ordering in *A*-site cations. The layered partial ordering magnitude is chosen to be similar to our optimized experimental values. Interestingly, the conduction band edge along the Γ→Z remains non-dispersive compared to Γ→X and Γ→M in partially ordered films, which suggests robustness of these 2D states against deviation from the perfect layered ordering.

Finally, we address the magnetic interactions and 2D spin-polarized states in $EuTa_2O_6$. The nature of magnetic interactions between Eu 4*f* and the *d* orbital-derived conduction states has been studied extensively in cubic perovskites such as $EuTiO_3$.[63–65] Recent theoretical predictions point to Ruderman-Kittel-Kasuya-Yosida (RKKY) type interactions in $EuTa_2O_6$.[28] Comprehensive understanding of the magnetic interactions and testing of the proposed mechanisms require careful

magneto-transport experiments which will be the subject of the future studies.

In summary, we report the growth of high-quality ATa_2O_6 (A: Eu and Sr) thin films by MBE. X-ray diffraction reveals the presence of partially ordered ATa_2O_6 films with the *c*-axis oriented mainly along the out-of-plane. Cross-sectional HAADF-STEM does not show any extended defects, while confirming presence of layered europium vacancy ordering. In situ ARPES measurements confirm the formation of quasi-2D conduction bands, in agreement with the calculated band structures. Further experimentations are needed to test the potential of $EuTa_2O_6$ to realize magnetically controllable spin-polarized 2D states. The synthesis and characterization results point to novel *materials by design* opportunities for electronic applications.

3. Experimental Section

Thin Film Synthesis and Characterization: Epitaxial thin films of $EuTa_2O_6$ were grown using a modified Vecco Gen 10 MBE system, where the conventional SiC heater was replaced by 10 µm CO_2-laser from Epiray GmbH (THERMALAS Substrate heater). A molecular beam of TaO_2 (gas) flux was generated from an effusion cell containing Ta_2O_5 (Alfa Aesar, 99.993%) contained in an iridium crucible. TaO_2 is the most volatile species in the effusion cell temperature range relevant to film growth.[66] Europium was evaporated from a conventional effusion cell. Each metal/suboxide flux ($\approx 1.5 \times 10^{13}$ atoms cm^{-2} s^{-1}) was measured before growth using a quartz crystal microbalance (QCM) in addition to deposition of the binary metal oxides Eu_2O_3 on YSZ (111), SrO on YSZ (100), and TaO_2 on R-plane sapphire to confirm deposition rates by x-ray reflectivity film thickness measurements and RHEED-oscillations for SrO.[67] Nb:$SrTiO_3$ and $SrTiO_3$ (001) substrates were terminated following the procedure developed by Koster.[68]

Films were grown by sequential deposition (using computer-controlled MBE shutters) of a europium atomic monolayer followed by two atomic layers of TaO_2 (i.e., -EuO-TaO_2-TaO_2- ...), at substrate temperatures of 750–1100 °C as measured by an optical pyrometer operating at a wavelength of 7.5 µm. No additional oxidant, other than that emitted by the Ta_2O_5 suboxide source, was used. The films were grown at a background pressure of 3×10^{-8} Torr. After deposition of each EuO-TaO_2-TaO_2 cycle a holding time of 100 s at growth temperature was employed before the next cycle.

X-ray diffraction (XRD), X-ray reflectometry (XRR), and RSM measurements were carried out using a PANalytical Empyrean diffractometer with Cu K_{α_1} radiation. The raw XRR spectra were analyzed using the PANalytical X´Pert Reflectivity software package, and the layer thickness was derived from a fast Fourier transform (FFT) after manually defining the critical angle to account for refractive effects. In situ reflection high-energy electron diffraction (RHEED) patterns were recorded using KSA-400 software and a Staib electron source operated at 14 kV and a filament current of 1.5 A. The morphology of the film surface was characterized using an Asylum Cypher ES environmental AFM.

Transmission Electron Microscopy: Cross-sectional samples for scanning transmission electron microscopy (S/TEM) analysis were prepared by employing a focused ion beam (FIB) lift-out technique using an FEI Helios NanoLab 600 DualBeam instrument. Initial thinning of the samples was performed with a 5 kV Ga-ion beam, followed by a final gentle polishing step at 2 kV to minimize surface damage. High-angle annular dark-field (HAADF) STEM imaging was conducted using a Thermo Fisher Scientific Themis-Z microscope operating at an accelerating voltage of 200 kV with a semi-convergence angle of 30 mrad. Images were acquired using a HAADF detector with a collection angle range of 64–200 mrad. To improve image quality and signal-to-noise ratio, high-resolution HAADF-STEM images were obtained by averaging 20 rapidly scanned frames (each 2048 × 2048 pixels, with 200 ns dwell time per pixel).

Angle-Resolved Photoemission Spectroscopy and X-Ray Photoelectron Spectroscopy: In situ ARPES measurements were performed at room temperature in an analysis chamber with base pressure better than 5×10^{-11} Torr using a Scienta Omicron DA30-L electron analyzer and a Fermion Instruments BL1200s plasma discharge lamp generating Ne-I (16,85 eV), He-Iα (21.2 eV), He-Iβ (23.09 eV), or Ne-II (26.9 eV) light. Ne-I and Ne-II spectra are processed with an algorithm described elsewhere to remove overlapping doublet spectra.[63] In situ X-ray photoelectron spectroscopy (XPS) were performed in the same chamber using a non-monochromated Scienta Omicron DSX400 x-ray source. Spectra were analyzed with an Omicron Sphera II analyzer after excitation.

Synchrotron Based Reciprocal Space Mapping: Reciprocal space mapping to characterize the structure of the $EuTa_2O_6$ films was performed using hard x-ray diffraction at the QM2 beamline of the Cornell High Energy Synchrotron Source (CHESS). Samples were mounted on a four-circle Huber diffractometer in reflection geometry with the sample normal oriented along the ϕ axis. With goniometer tilts of omega = 3° and $\chi = 90°$, diffraction images were collected on a Pilatus 6M detector using 18 keV incident X-rays while continuously rotating ϕ through 360° degrees in 0.1°degree steps with a 0.1 s counting time per image. Polarization and Lorentz factor corrections were applied to the raw images which were transformed into a 3D reciprocal space map. Line scans along the crystal truncation rods (CTR) were extracted from the 3D reciprocal space maps. Gaps between detector panels result in small sections of missing data in the CTRs. The sharp and relatively weak peaks are $SrTiO_3$ substrate diffraction peaks from higher order x-ray harmonics unfiltered by the monochromator; they should not be confused with $EuTa_2O_6$ Bragg peaks. Miller indices *H*, *K*, and *L* refer to the $2 \times 2 \times 2$ pseudo cubic perovskite unit cell of $Eu_{0.5}TaO_3$.

Density Functional Theory: Density functional theory (DFT) calculations were performed using the Vienna Ab initio Simulation Package (VASP).[69,70] The Projector Augmented Wave (PAW) method was employed, with the exchange-correlation functional treated through the meta-generalized gradient approximation (MetaGGA) for structure relaxation, utilizing the Regularized-Restored Strongly Constrained and Appropriately Normed (r^2SCAN) formulation.[71] For the band structure calculations, the generalized gradient approximation (GGA) with the Perdew–Burke–Ernzerhof (PBE) formulation[72] was applied. The kinetic cutoff energy was set to be 450 eV. For structure optimization, the Brillouin zone was sampled with an $8 \times 8 \times 6$ k-mesh, while a $12 \times 12 \times 10$ k-mesh was used for self-consistent field calculations. To capture the strong correlation effects of the localized Ta 5*d* and Eu 4*f* orbitals, the DFT + *U* approach developed by Dudarev et al.[73] was utilized. This involved adding an onsite Hubbard *U* term and an exchange correction J, resulting in an effective value of $U_{eff} = U\text{-}J = 7$ eV for tantalum and 5 eV for europium. Relativistic effects, including spin-orbit coupling, were fully incorporated. A $2 \times 2 \times 1$ supercell was constructed to simulate the disordered $Eu_{0.5}TaO_3$ structure. To model the random 50–50% europium occupancy, two europium atoms were placed in the first layer, and the remaining two were placed in the second layer. After optimizing the structure, the band structure was calculated. The presence of europium atoms in the middle layer altered the positions of the tantalum atoms, eliminating the distortions.

Supporting Information

Supporting Information is available from the Wiley Online Library or from the author.

Acknowledgements

This work made use of the synthesis and ARPES facilities of the Platform for the Accelerated Realization, Analysis, and Discovery of Interface Materials (PARADIM), which are supported by the National Science Foundation under Cooperative Agreement No. DMR-2039380. K.A., M.G., P.M.W., and S.S.-R. acknowledge support from a Strategic Research Initiative Grant of College of Engineering at the Ohio State University. KA also acknowledges discussions with M.-S. Bahramy. S.S.-R. acknowledges Dan

Huber for assisting with TEM sample preparation. Electron microscopy was performed at the Center for Electron Microscopy and Analysis (CEMAS) at The Ohio State University. T.S. and D.G.S. acknowledge support from the National Science Foundation (NSF) under No. DMR-2039380. P. M. W., A.B., and M.G. acknowledge support from the Center for Emergent Materials (CEM), a National Science Foundation MRSEC under NSF Award Number DMR-2011876. J.W.H, B.Z.G., and A.S., acknowledge support from for the measurement and interpretation of 3D reciprocal space maps from the U.S. Department of Energy, Office of Science, Office of Basic Energy Sciences, under Contract No. DE-SC0019414.This work made use of the Cornell Center for Materials Research (CCMR) Shared Facilities, which are supported through the NSF MRSEC Program No. DMR-1719875. This work made use of the Cornell Center for Materials Research (CCMR) Shared Facilities, which are supported through the NSF MRSEC Program (Grant No. DMR-1719875). The authors acknowledge Steve Button for substrate preparation.

Conflict of Interest

The authors declare no conflict of interest.

Data Availability Statement

The data that support the findings of this study are openly available in [PARADIM (https://data.paradim.org/doi/10.34863/zs70-r236)] at [https://doi.org/10.34863/zs70-r236].

Keywords

2D electronics, double perovskite, $EuTa_2O_6$, fractional double perovskites, oxide molecular beam epitaxy

Received: June 2, 2025
Revised: July 28, 2025
Published online:

[1] A. C. Gossard, in *Molecular Beam Epitaxy and Heterostructures* (Eds.: L. L. Chang, K. Ploog), Springer, Berlin, Germany **1985**, pp. 499–531.
[2] H. Kroemer, *Rev. Mod. Phys.* **2001**, *73*, 783.
[3] D. C. Tsui, H. L. Stormer, A. C. Gossard, *Phys. Rev. Lett.* **1982**, *48*, 1559.
[4] R. Willett, J. P. Eisenstein, H. L. Störmer, D. C. Tsui, A. C. Gossard, J. H. English, *Phys. Rev. Lett.* **1987**, *59*, 1776.
[5] H. L. Stormer, A. Chang, D. C. Tsui, J. C. M. Hwang, A. C. Gossard, W. Wiegmann, *Phys. Rev. Lett.* **1983**, *50*, 1953.
[6] K. V. Klitzing, G. Dorda, M. Pepper, *Phys. Rev. Lett.* **1980**, *45*, 494.
[7] Y. Cao, V. Fatemi, S. Fang, K. Watanabe, T. Taniguchi, E. Kaxiras, P. Jarillo-Herrero, *Nature* **2018**, *556*, 43.
[8] Y. Saito, T. Nojima, Y. Iwasa, *Nat. Rev. Mater.* **2016**, *2*, 16094.
[9] R. Ramesh, N. A. Spaldin, *Nat. Mater.* **2007**, *6*, 21.
[10] J. Mannhart, D. G. Schlom, *Science* **2010**, *327*, 1607.
[11] M. Coll, J. Fontcuberta, M. Althammer, M. Bibes, H. Boschker, A. Calleja, G. Cheng, M. Cuoco, R. Dittmann, B. Dkhil, I. El Baggari, M. Fanciulli, I. Fina, E. Fortunato, C. Frontera, S. Fujita, V. Garcia, S. T. B. Goennenwein, C.-G. Granqvist, J. Grollier, R. Gross, A. Hagfeldt, G. Herranz, K. Hono, E. Houwman, M. Huijben, A. Kalaboukhov, D. J. Keeble, G. Koster, L. F. Kourkoutis, et al., *Appl. Surf. Sci.* **2019**, *482*, 1.
[12] D. G. Schlom, *APL Mater.* **2015**, *3*, 062403.
[13] Y. F. Nie, P. D. C. King, C. H. Kim, M. Uchida, H. I. Wei, B. D. Faeth, J. P. Ruf, J. P. C. Ruff, L. Xie, X. Pan, C. J. Fennie, D. G. Schlom, K. M. Shen, *Phys. Rev. Lett.* **2015**, *114*, 016401.
[14] J. M. Rondinelli, S. J. May, J. W. Freeland, *MRS Bull.* **2012**, *37*, 261.
[15] S. Stemmer, S. J Allen, *Annu. Rev. Mater. Res.* **2014**, *44*, 151.
[16] S. Stemmer, A. J. Millis, *MRS Bull.* **2013**, *38*, 1032.
[17] N. Reyren, S. Thiel, A. D. Caviglia, L. F. Kourkoutis, G. Hammerl, C. Richter, C. W. Schneider, T. Kopp, A.-S. Rüetschi, D. Jaccard, M. Gabay, D. A. Muller, J.-M. Triscone, J. Mannhart, *Science* **2007**, *317*, 1196.
[18] C. Liu, X. Yan, D. Jin, Y. Ma, H.-W. Hsiao, Y. Lin, T. M. Bretz-Sullivan, X. Zhou, J. Pearson, B. Fisher, J. S. Jiang, W. Han, J.-M. Zuo, J. Wen, D. D. Fong, J. Sun, H. Zhou, A. Bhattacharya, *Science* **2021**, *371*, 716.
[19] J. Falson, D. Maryenko, B. Friess, D. Zhang, Y. Kozuka, A. Tsukazaki, J. H. Smet, M. Kawasaki, *Nat. Phys.* **2015**, *11*, 347.
[20] L. Li, C. Richter, J. Mannhart, R. C. Ashoori, *Nat. Phys.* **2011**, *7*, 762.
[21] P. Moetakef, J. R. Williams, D. G. Ouellette, A. P. Kajdos, D. Goldhaber-Gordon, S. J. Allen, S. Stemmer, *Phys. Rev. X* **2012**, *2*, 021014.
[22] K. Ahadi, S. Stemmer, *Phys. Rev. Lett.* **2017**, *118*, 236803.
[23] D. C. Vaz, P. Noël, A. Johansson, B. Göbel, F. Y. Bruno, G. Singh, S. McKeown-Walker, F. Trier, L. M. Vicente-Arche, A. Sander, S. Valencia, P. Bruneel, M. Vivek, M. Gabay, N. Bergeal, F. Baumberger, H. Okuno, A. Barthélémy, A. Fert, L. Vila, I. Mertig, J.-P. Attané, M. Bibes, *Nat. Mater.* **2019**, *18*, 1187.
[24] E. Lesne, Y. Fu, S. Oyarzun, J. C. Rojas-Sánchez, D. C. Vaz, H. Naganuma, G. Sicoli, J.-P. Attané, M. Jamet, E. Jacquet, J.-M. George, A. Barthélémy, H. Jaffrès, A. Fert, M. Bibes, L. Vila, *Nat. Mater.* **2016**, *15*, 1261.
[25] A. D. Caviglia, M. Gabay, S. Gariglio, N. Reyren, C. Cancellieri, J.-M. Triscone, *Phys. Rev. Lett.* **2010**, *104*, 126803.
[26] E. Lesne, Y. G. Sağlam, R. Battilomo, M. T. Mercaldo, T. C. van Thiel, U. Filippozzi, C. Noce, M. Cuoco, G. A. Steele, C. Ortix, A. D. Caviglia, *Nat. Mater.* **2023**, *22*, 576.
[27] K. Ahadi, H. Kim, S. Stemmer, *APL Mater.* **2018**, *6*, 056102.
[28] O. Dowinton, D. Maryenko, R. V. Belosludov, B. Yang, M. S. Bahramy, *Adv Funct. Mater.* **2023**, *33*, 2300995.
[29] K. J. Choi, M. Biegalski, Y. L. Li, A. Sharan, J. Schubert, R. Uecker, P. Reiche, Y. B. Chen, X. Q. Pan, V. Gopalan, L. Q. Che, D. C. Schlom, C. B. Eom, *Science* **2004**, *306*, 1005.
[30] J. H. Lee, L. Fang, E. Vlahos, X. Ke, Y. W. Jung, L. F. Kourkoutis, J. W. Kim, P. J. Ryan, T. Heeg, M. Roeckerath, V. Goian, M. Bernhagen, R. Uecker, P. C. Hammel, K. M. Rabe, S. Kamba, J. Schubert, J. W. Freeland, D. A. Muller, C. J. Fennie, P. Schiffer, V. Gopalan, E. Johnston-Halperin, D. G. Schlom, *Nature* **2010**, *466*, 954.
[31] S. Vasala, M. Karppinen, *Prog. Solid State Chem.* **2015**, *43*, 1.
[32] C. J. Howard, B. J. Kennedy, P. M. Woodward, *Acta Crystallograph. Sect. B: Struct. Sci.* **2003**, *59*, 463.
[33] M. T. Anderson, K. B. Greenwood, G. A. Taylor, K. R. Poeppelmeier, *Prog. Solid State Chem.* **1993**, *22*, 197.
[34] P. K. Davies, H. Wu, A. Y. Borisevich, I. E. Molodetsky, L. Farber, *Annu. Rev. Mater. Res.* **2008**, *38*, 369.
[35] G. King, P. M. Woodward, *J. Mater. Chem.* **2010**, *20*, 5785.
[36] F. Millange, V. Caignaert, B. Domengès, B. Raveau, E. Suard, *Chem. Mater.* **1998**, *10*, 1974.
[37] S. Yamada, Y. Maeda, T. Arima, *J. Phys. Soc. Jpn.* **2012**, *81*, 113711.
[38] D. G. Schlom, L.-Q. Chen, C.-B. Eom, K. M. Rabe, S. K. Streiffer, J.-M. Triscone, *Annu. Rev. Mater. Res.* **2007**, *37*, 589.
[39] S. Hazra, T. Schwaigert, A. Ross, H. Lu, U. Saha, V. Trinquet, B. Akkopru-Akgun, B. Z. Gregory, A. Mangu, S. Sarker, T. Kuznetsova, S. Sarker, X. Li, M. R. Barone, X. Xu, J. W. Freeland, R. Engel-Herbert, A. M. Lindenberg, A. Singer, S. Trolier-McKinstry, D. A. Muller, G. Rignanese, S. Salmani-Rezaie, V. A. Stoica, A. Gruverman, L. Chen, D. G. Schlom, V. Gopalan, *Adv. Mater.* **2024**, *36*, 2408664.
[40] J. H. Haeni, P. Irvin, W. Chang, R. Uecker, P. Reiche, Y. L. Li, S. Choudhury, W. Tian, M. E. Hawley, B. Craigo, A. K. Tagantsev, X. Q.

Pan, S. K. Streiffer, L. Q. Chen, S. W. Kirchoefer, J. Levy, D. G. Schlom, *Nature* **2004**, *430*, 758.
[41] D. O. Klenov, W. Donner, B. Foran, S. Stemmer, *Appl. Phys. Lett.* **2003**, *82*, 3427.
[42] W. Donner, C. Chen, M. Liu, A. J. Jacobson, Y.-L. Lee, M. Gadre, D. Morgan, *Chem. Mater.* **2011**, *23*, 984.
[43] V. Sirotinkin, S. Sirotinkin, V. Trunov, *Zhurnal Neorganicheskoj Khimii* **1989**, *34*, 803.
[44] S. Ebisu, H. Morita, S. Nagata, *J. Phys. Chem. Solids* **2000**, *61*, 45.
[45] Q. Zhou, P. J. Saines, N. Sharma, J. Ting, B. J. Kennedy, Z. Zhang, R. L. Withers, K. S. Wallwork, *Chem. Mater.* **2008**, *20*, 6666.
[46] D. J. Scalapino, *Phys. Rep.* **1995**, *250*, 329.
[47] Y. Maeno, K. Yoshida, H. Hashimoto, S. Nishizaki, S. Ikeda, M. Nohara, T. Fujita, A. P. Mackenzie, N. E. Hussey, J. G. Bednorz, F. Lichtenberg, *J. Phys. Soc. Jpn.* **1997**, *66*, 1405.
[48] F. Lichtenberg, A. Catana, J. Mannhart, D. G. Schlom, *Appl. Phys. Lett.* **1992**, *60*, 1138.
[49] L. Zhang, J. Chen, L. Fan, O. Diéguez, J. Cao, Z. Pan, Y. Wang, J. Wang, M. Kim, S. Deng, J. Wang, H. Wang, J. Deng, R. Yu, J. F. Scott, X. Xing, *Science* **2018**, *361*, 494.
[50] K. Inaba, S. Suzuki, Y. Noguchi, M. Miyayama, *J. Alloys Compd.* **2009**, *486*, 78.
[51] B. J. Campbell, H. T. Stokes, D. E. Tanner, D. M. Hatch, *J. Appl. Crystallogr.* **2006**, *39*, 607.
[52] M. C. Knapp, P. M. Woodward, *J. Solid State Chem.* **2006**, *179*, 1076.
[53] N. Nakagawa, H. Y. Hwang, D. A. Muller, *Nat. Mater.* **2006**, *5*, 204.
[54] T. Schwaigert, S. Salmani-Rezaie, M. R. Barone, H. Paik, E. Ray, M. D. Williams, D. A. Muller, D. G. Schlom, K. Ahadi, *J. Vacuum Sci. Technol. A* **2023**, *41*, 022703.
[55] S. Hasko, A. Tenneti, T. Schwaigert, https://github.com/Stunion235/POMMES (accessed: November 2024).
[56] F. Izumi, K. Momma, *Solid State Phenomena* **2007**, *130*, 15.
[57] K. Momma, F. Izumi, *J. Appl. Crystallogr.* **2008**, *41*, 653.
[58] A. Mariscal, A. Quesada, A. Tarazaga Martín-Luengo, M. A. García, A. Bonanni, J. F. Fernández, R. Serna, *Appl. Surf. Sci.* **2018**, *456*, 980.
[59] R. Vercaemst, D. Poelman, R. L. Van Meirhaeghe, L. Fiermans, W. H. Laflère, F. Cardon, *J. Lumin.* **1995**, *63*, 19.
[60] M. Khanuja, H. Sharma, B. R. Mehta, S. M. Shivaprasad, *J. Electron Spectrosc. Relat. Phenom.* **2009**, *169*, 41.
[61] A. X. Wei, Z. X. Ge, X. H. Zhao, J. Liu, Y. Zhao, *J. Alloys Compd.* **2011**, *509*, 9758.
[62] R. J. D. Tilley, *Perovskites: Structure-Property Relationships*, Wiley, Hoboken, New Jersey **2016**.
[63] K. Ahadi, Z. Gui, Z. Porter, J. W. Lynn, Z. Xu, S. D. Wilson, A. Janotti, S. Stemmer, *APL Mater.* **2018**, *6*, 056105.
[64] K. Ahadi, L. Galletti, S. Stemmer, *Appl. Phys. Lett.* **2017**, *111*, 172403.
[65] K. Ahadi, X. Lu, S. Salmani-Rezaie, P. B. Marshall, J. M. Rondinelli, S. Stemmer, *Phys. Rev. B* **2019**, *99*, 041106.
[66] K. M. Adkison, S.-L. Shang, B. J. Bocklund, D. Klimm, D. G. Schlom, Z.-K. Liu, *APL Mater.* **2020**, *8*, 081110.
[67] J. Sun, C. T. Parzyck, J. H. Lee, C. M. Brooks, L. F. Kourkoutis, X. Ke, R. Misra, J. Schubert, F. V. Hensling, M. R. Barone, Z. Wang, M. E. Holtz, N. J. Schreiber, Q. Song, H. Paik, T. Heeg, D. A. Muller, K. M. Shen, D. G. Schlom, *Phys. Rev. Mater.* **2022**, *6*, 033802.
[68] G. Koster, B. L. Kropman, G. J. H. M. Rijnders, D. H. A. Blank, H. Rogalla, *Appl. Phys. Lett.* **1998**, *73*, 2920.
[69] G. Kresse, J. Furthmüller, *Comput. Mater. Sci.* **1996**, *6*, 15.
[70] G. Kresse, J. Furthmüller, *Phys. Rev. B* **1996**, *54*, 11169.
[71] J. W. Furness, A. D. Kaplan, J. Ning, J. P. Perdew, J. Sun, *J. Phys. Chem. Lett.* **2020**, *11*, 8208.
[72] J. P. Perdew, K. Burke, M. Ernzerhof, *Phys. Rev. Lett.* **1996**, *77*, 3865.
[73] S. L. Dudarev, G. A. Botton, S. Y. Savrasov, C. J. Humphreys, A. P. Sutton, *Phys. Rev. B* **1998**, *57*, 1505.

ADVANCED FUNCTIONAL MATERIALS

Supporting Information

for *Adv. Funct. Mater.*, DOI 10.1002/adfm.202513656

Synthesis and Electronic Structure of the Fractionally Occupied Double Perovskite $EuTa_2O_6$ with Ordered Europium Vacancies

*Tobias Schwaigert, Ali Barooni, Benjamin Gregory, Paul Malinowski, Anirudh Tenneti, Sonia Hasko, Brenan Palazzolo, Jeffrey W Hodgson, Brendan Faeth, Patrick M. Woodward, Kyle M. Shen, Andrej Singer, Maryam Ghazisaeidi, Salva Salmani-Rezaie, Darrell G. Schlom and Kaveh Ahadi**

Supporting Information

Synthesis and electronic structure of the fractionally occupied double perovskite $EuTa_2O_6$ with ordered europium vacancies

Tobias Schwaigert[1], Ali Barooni[2], Benjamin Gregory[3,4], Paul Malinowski[3], Anirudh Tenneti[1], Sonia Hasko[5,6], Brenan Palazzolo[5,7]Jeffrey W Hodgson[1], Brendan Faeth[5], Patrick M. Woodward[8], Kyle M. Shen[3,4], Andrej Singer[1], Maryam Ghazisaeidi[2], Salva Salmani-Rezaie[2], Darrell G. Schlom[1,9,10], Kaveh Ahadi[2,*]

1: Department of Materials Science and Engineering, Cornell University, Ithaca, New York 14853, USA

2: Department of Materials Science and Engineering, The Ohio State University, Columbus, Ohio 43210, USA

3: Department of Physics, Cornell University, Ithaca, New York 14853, USA

4: Laboratory of Atomic and Solid State Physics, Department of Physics, Cornell University, Ithaca, NY, USA.

5: Platform for the Accelerated Realization, Analysis, and Discovery of Interface Materials (PARADIM), Cornell University, Ithaca, New York 14853, USA

6: Department of Chemical and Biological Engineering, Princeton University, Princeton, NJ, USA

7: Department of Physics and Astronomy, Clemson University, Clemson, SC 29631, USA

8: Department of Chemistry, The Ohio State University, Columbus, Ohio 43210, USA

9: Kavli Institute at Cornell for Nanoscale Science, Ithaca, New York 14853, USA

10: Leibniz-Institut für Kristallzüchtung, Max-Born-Straße 2, 12489 Berlin, Germany

[*] Corresponding author. Email: ahadi.4@osu.edu

1. Fermi Surface calculation of $EuTa_2O_6$.

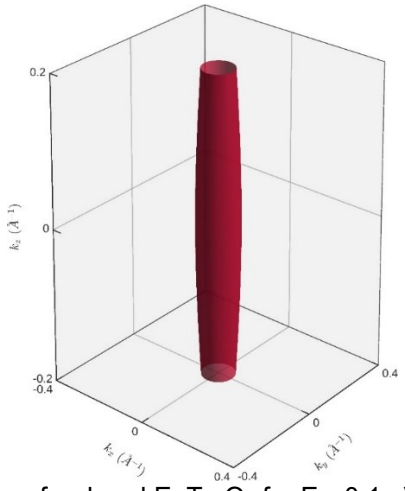

Figure S1: Calculated Fermi Surface of ordered $EuTa_2O_6$ for E_F=0.1 eV, exhibiting 2D electronic states due to Ta^{5+} d_{xy} character.

2. Exploration of phase stability during Synthesis

Additional samples were grown to explore the stability window during thin film deposition. Multiple growth parameters were systematically changed to optimize vacancy ordering. **Figure S3** shows the impact of holding after a cycle of Eu and Ta is deposited. With increased time, the intensity of ordering peaks increases, indicating the formation of $EuTa_2O_6$ rather than the disordered $Eu_{0.5}TaO_3$. While vacancy order increases, Laue oscillations around film peaks persist, indicating a smooth interface between film and substrate. Varrying the Eu shutter time impacts sample quality the least out of all the varied parameters. With increased shutter time beyond on 1 monolayer of Eu, the onset of ordering can be observed (**Fig. S3**). A maximum is observed at 1.06 M.L. Conversely, increasing the shutter time of Ta beyond 1 monolayer initially increases the intensity of ordering peaks, however, the intensity of fundamental peaks decreases, in addition to the vanishing of Laue oscillations, indicating that the film quality is decreasing (**Fig. S4**). Lastly the temperature was varied in two regimes: I. stoichiometric conditions, II. Optimized shutter times to maximize ordering. **Figure S5** shows the impact of temperature on stoichiometric samples. The optimal temperature is 800 °C, where film quality is adequate, while ordering peaks are clearly visible. Increasing the temperature to 850 °C causes the ordering peak to vanish, while shifting the fundamental peaks towards smaller lattice constants. **Figure S6** shows films grown under optimized growth conditions determined from previous experiments (**Fig S2-4**). Here, ordering peaks are present throughout a larger range temperatures, beyond the point of phase stability. At 1000°C and above Eu-oxide starts to segregate, with an intermediate unknown phase at 31.12°, increasing the temperature further EuO 111 (29.77°)[1] dominates.

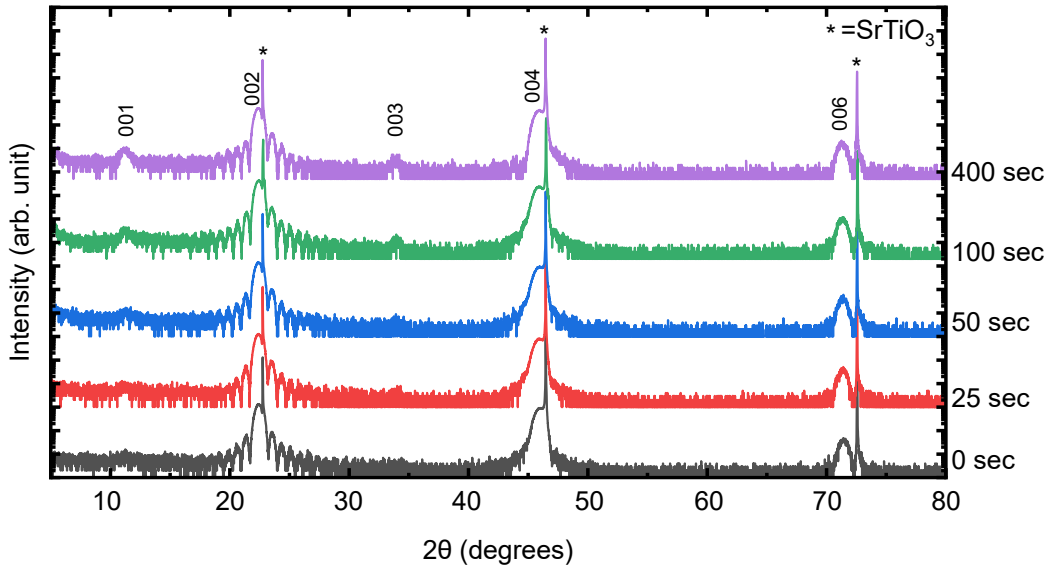

Figure S2: Impact of holding time on $EuTa_2O_6$ thin film growth. All films are grown at a substrate temperature of 800°C with Eu and Ta_2O_5 shutter times that correspond to a 1:1 stoichiometry ratio, while also maintaining a monolayer-by-monolayer deposition time. The onset of ordering can be observed above 50 seconds of holding time.

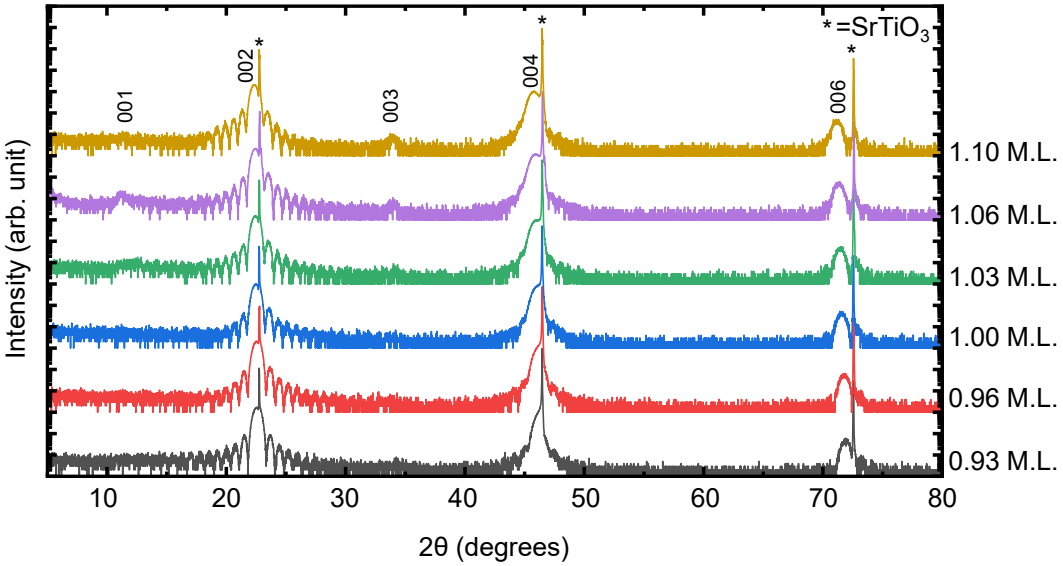

Figure S3: Impact of Eu-Stoichiometry during deposition. All films are grown at a substrate temperature of 800°C, 100 second holding time after a cycle of Eu and Ta_2O_5 deposition. Ordering peaks (even-even-odd) have the highest intensity for 1.06 M.L. of Eu.

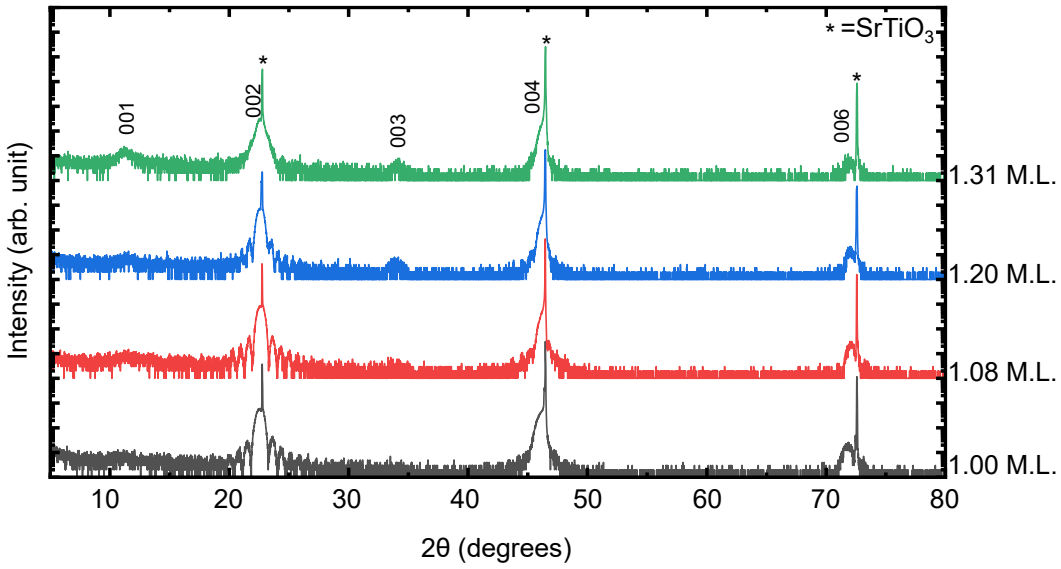

Figure S4: Impact of Ta_2O_5-Stoichiometry during deposition. All films are grown at a substrate temperature of 800°C, 100 second holding time after a cycle of Eu and Ta deposition. Eu deposition time was held constant (1 M.L.).

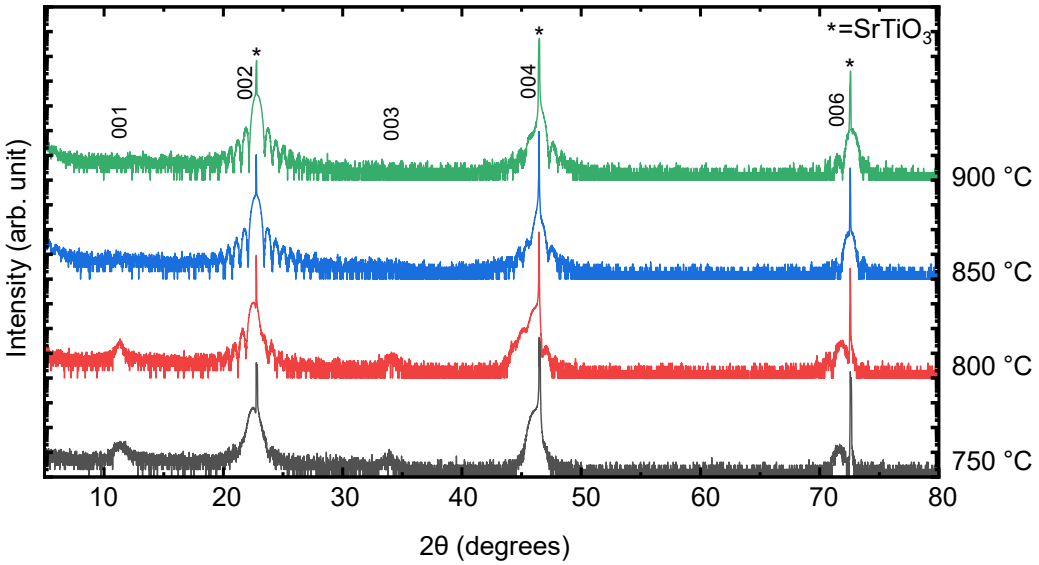

Figure S5: Impact of substrate temperature under stoichiometric conditions. All films are grown at with a 1:1 (Eu:Ta_2O_5) Stoichiometric ratio, 100 second holding time after a cycle of Eu and Ta deposition.

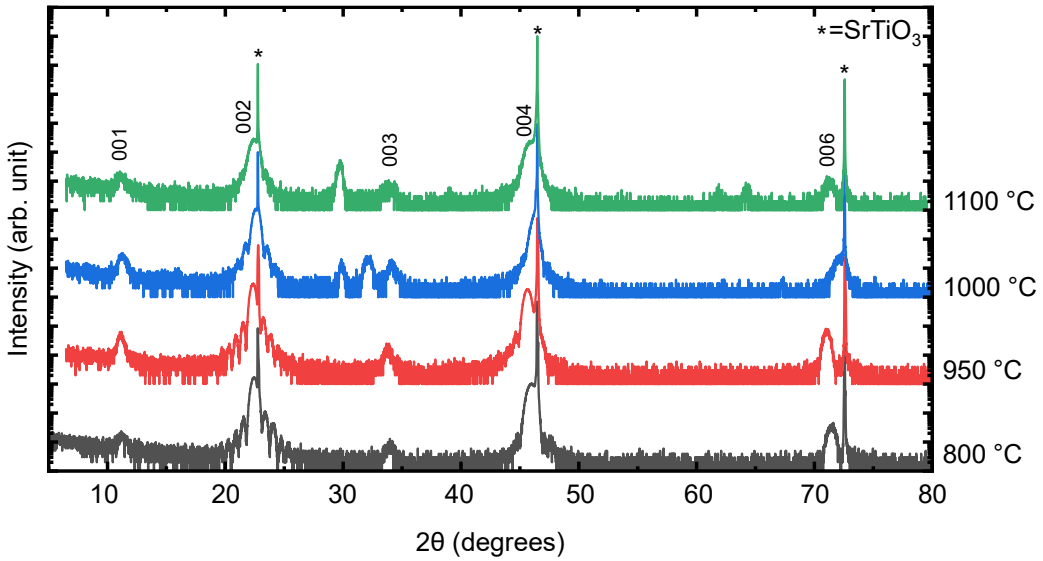

Figure S6: Impact of substrate temperature during deposition. All films are deposited with an increased Shutter time of Eu (1.06 M.L.) and Ta_2O_5 (1.20 M.L), 100 seconds holding time after a cycle of Eu and Ta.

3. Additional Sample characterization for $EuTa_2O_6$ on Nb:$SrTiO_3$

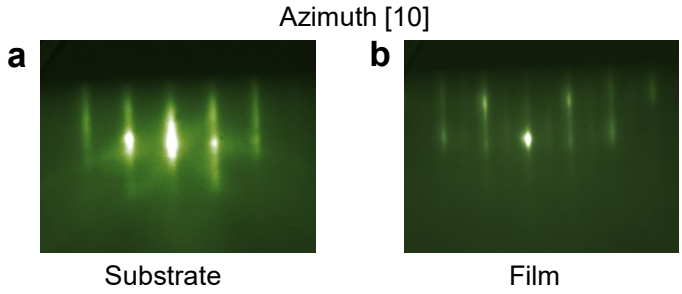

Figure S7: RHEED patterns of **a** bare $SrTiO_3$ substrate; **b** 16 nm thick $EuTa_2O_6$ film on Nb:$SrTiO_3$ 001.

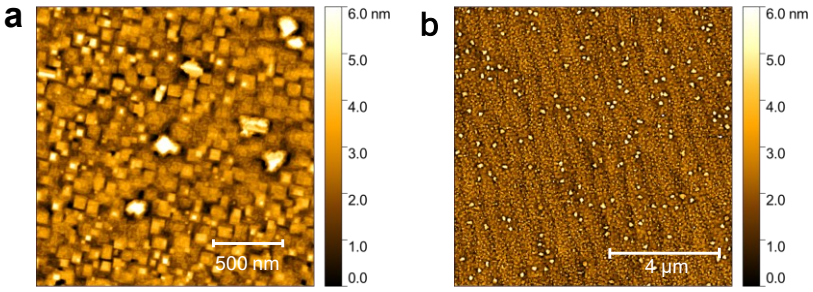

Figure S8: Atomic force microscopy images of a 16.3 nm thick film of $EuTa_2O_6$ on $SrTiO_3$ at different magnification, revealing atomic steps.

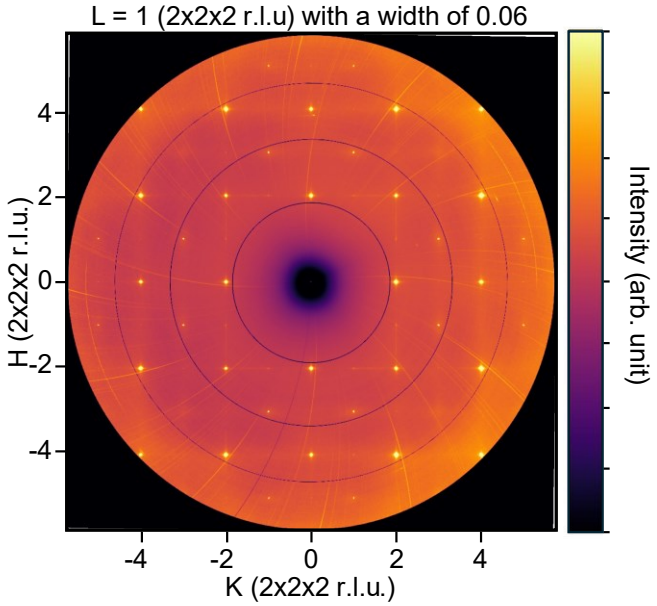

Figure S10: Hard x-ray reciprocal space mapping (L = 1) for a 16 nm thick $EuTa_2O_6$ film on Nb:$SrTiO_3$ (001) slices at 300 K.

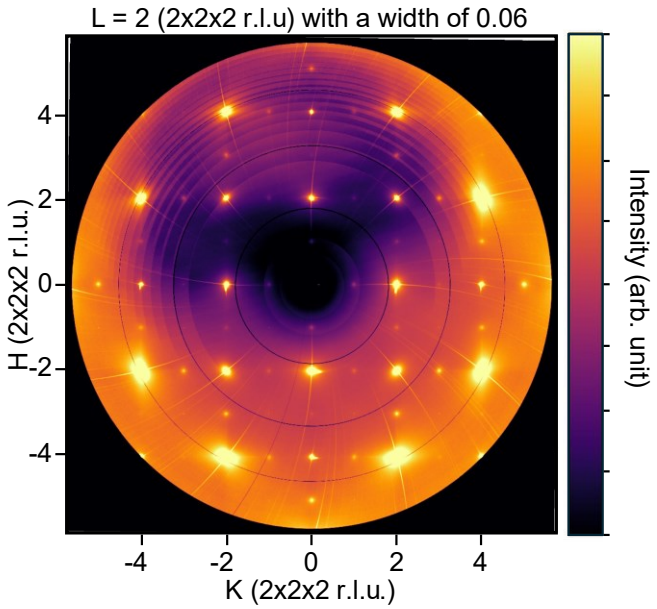

Figure S11: Hard x-ray reciprocal space mapping (L = 2) for a 16 nm thick $EuTa_2O_6$ film on Nb:$SrTiO_3$ (001) slices at 300 K.

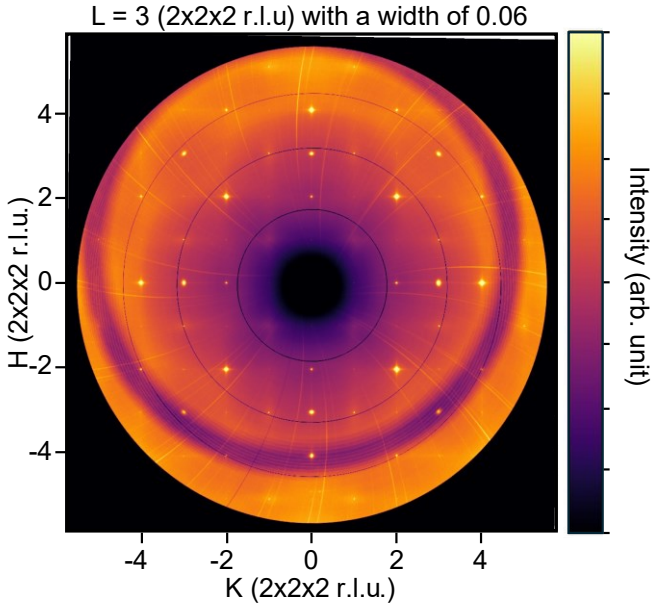

Figure S12: Hard x-ray reciprocal space mapping (L = 3) for a 16 nm thick $EuTa_2O_6$ film on Nb:$SrTiO_3$ (001) slices at 300 K.

Table S1: Symmetry analysis of octahedral tilting in a Perovskite with layered ordering of the A-site cations like $EuTa_2O_6$. The Unit cell of the parent structure is $a_p \approx 3.9$ Å and $c_p \approx 7.9$ Å.

Tilt system	Space group	Unit cell*	Notes about symmetry mode
$a^0a^0c^+$	P4/mbm	$\sqrt{2}a_p \times \sqrt{2}a_p \times c$	irrep = M_3^+, direction = P1 (parent $LaNb_3O_9$)
$a^0a^0c^-$	P4/nbm	$\sqrt{2}a_p \times \sqrt{2}a_p \times c$	irrep = M_1^-, direction = P1 (parent $LaNb_3O_9$)
$a^-b^0c^0$	Cmmm	$2a_p \times 2a_p \times c$	irrep = M_5^-, direction = P3 (parent $LaNb_3O_9$)
$a^-a^-c^0$	Pmma	$\sqrt{2}a_p \times c \times \sqrt{2}a_p$	irrep = X_2^-, direction = P1 (parent $BaPbO_3$)

3. Quantifying order through structure factor calculations

To quantify the order parameter of thin films of ETO, we doubled the unit cell of $Eu_{0.5}TaO_3$ and changed the occupancy, *x*, of the europium atoms. This helped us simulate the behavior of the fractional double perovskite, $Eu_xTa_{2x}O_{6x}$, where $0.5 \leq x \leq 1.0$. When $x = 0.5$, ETO is in its most disordered form: $Eu_{0.5}TaO_3$. The unit cell of this form of ETO is cubic. Conversely, when x = 1.0, ETO exists in its most ordered form: $EuTa_2O_6$. DFT was used to predict the structure of ETO, which was the basis for the theoretical XRD peak intensity calculations done for a wide range of occupancy values. Intensity ratios obtained from experimental data were compared to the theoretical intensity ratio curves to quantify the occupancy of europium in ETO thin films.

The most ordered form of ETO, $EuTa_2O_6$, crystallizes as a tetragonal structure in the *P4/mmm* space group. This crystal has been refined by structural relaxation in DFT calculations, resulting in lattice constants of $a = b = 3.9257$ Å, $c = 7.9293$ Å. The following atomic position basis is based on the DFT calculations:

Eu1 = [0.0, 0.0, 0.0]
Eu2 = [0.0, 0.0, 0.50000]

Ta1 = [0.50000,0.50000, z_{Ta}]
Ta2 = [0.50000, 0.50000, 1-z_{Ta}]

O1 = [0.50000, 1.0000, z_{O1}]
O2 = [0.50000, 0.0, 1- z_{O1}]
O3 = [0.0, 0.50000, z_{O3}]
O4 = [1.0000, 0.50000, 1- z_{O3}]

O5 = [0.50000, 0.50000, 1.0000]
O6 = [0.50000, 0.50000, 0.50000]

Three additional atomic positions – Ta2, O2, and O4 – were added to the Python code to account for the stoichiometry of the unit cell. The Python code does not consider symmetry; therefore, the entire position basis must be entered. Eu2 is present in the crystal only if the occupancy of Eu1 is less than 1.0. The occupancies of Eu1 and Eu2 sum to 1.0.

The values of z_{Ta}, z_{O1}, and z_{O3} are occupancy-dependent: as the occupancy *x* of the Eu1 layer increases in the fractional perovskite $Eu_xTa_{2x}O_{6x}$, the tantalum and oxygen atoms are displaced along the *c*-axis of the doubled unit cell (**Figure 1 a**). The displacements allow for the atoms to occupy optimal positions for charge transfer. In the most ordered state ($x = 1.0$), the *z*-positions are equal to those reported in the DFT calculations. These calculations account for Ta^{5+} polarization and the resultant Ta and O displacements:

$z_{Ta} = 0.25966$
$z_{O1} = 0.22992$
$z_{O3} = 0.22999$

The ordered $EuTa_2O_6$ structure is distinct from the fully disordered $Eu_{0.5}TaO_3$ structure. The latter crystallizes in the $Pm\bar{3}m$ space group with lattice constants of $a = b = c = 3.9257$ Å. In the disordered unit cell, the equal distribution of europium atoms in each plane is signified by a 50 % occupancy of each Eu atom. As a result, Ta^{5+} ions are no longer displaced towards the vacancy layer, lowering the SOJT elongation of the polyhedra. When accounting for the lack of displacements, the occupancy-dependent *z*-positions become equivalent:

$$z_{Ta} = z_{O1} = z_{O3} = 0.25$$

To calculate theoretical XRD intensity ratios, atomic form factors for each distinct atom or ion in the crystal must be computed. The atomic form factors, which are dependent on the lattice constants of the crystal, were computed for each ion or atom using the formula[2]

$$f(|\vec{G}|) = c_0 + \sum_{i=1}^{4} a_i \exp\left(-b_i \left(\frac{G}{4\pi}\right)^2\right)$$

where $G = |\vec{G}|$ and is calculated as follows:

$$G = \frac{2\pi}{d}$$

$$d = \frac{1}{\sqrt{\left(\frac{h}{a}\right)^2 + \left(\frac{k}{b}\right)^2 + \left(\frac{l}{c}\right)^2}}$$

a_i, b_i, and c_0 are angle-dependent empirical fitting parameters that are tabulated in the International Tables for Crystallography. Specifically, the parameters for the ions Eu^{2+} and Ta^{5+} and for the free atom O were used in the above calculations. The parameters have been calculated using relativistic Dirac-Slater wavefunctions (Ta^{5+}, Eu^{2+}) and relativistic Hartree-Fock wavefunctions (O).
Structure factors were subsequently calculated as follows:

$$S_{hkl}(x) = xF_{Eu1} + (1-x)F_{Eu2} + F_{Ta} + F_O$$

$$F = f_j(|\vec{G}|) \sum_{j=1}^{n} \exp\left(2\pi i(hx_j + ky_j + lz_j)\right)$$

where x is the occupancy of Eu1, and n corresponds to the number of atoms of the same element in the atomic position basis that share an occupancy value.

To validate this approach, structure factors of the extensively studied cubic perovskite $SrTiO_3$ were calculated. The close match between the calculated $SrTiO_3$ structure factors and the VESTA-generated $SrTiO_3$ structure factors suggested that the approach is accurate.

To further validate the use of our Python code on ETO, the structure factors of ETO were calculated using the code, then compared to VESTA-generated structure factors.

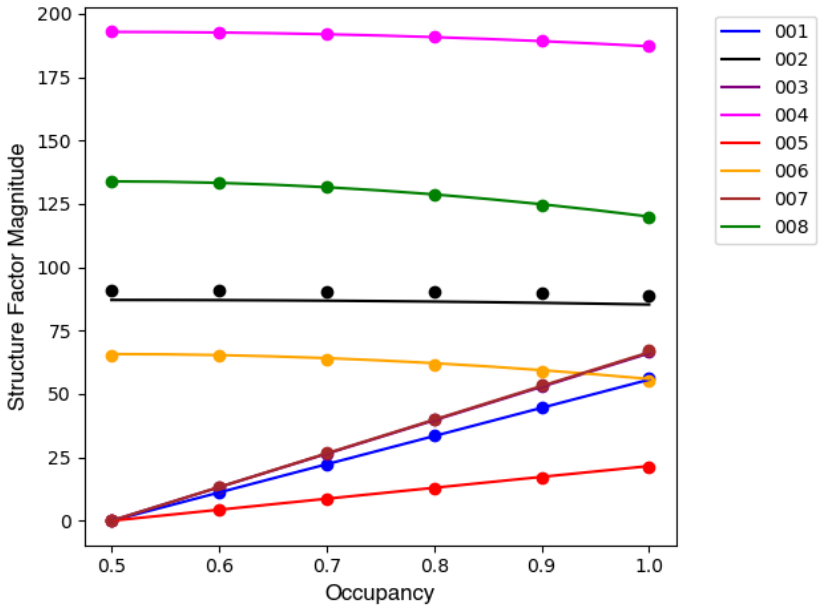

Figure S12: Calculated structure factors for ETO using the DFT-based atomic position basis are plotted against structure factors generated by VESTA software for the *P4/mmm* ETO crystal. Structure factors for the (001) through (008) peaks are shown here. Calculations were iteratively done for $0.5 \leq x \leq 1.0$ using Python code, whereas VESTA structure factors were found for selected occupancy values in the same range. Miller indices are based on the doubled unit cell of ETO.

After validating our method for calculating structure factors, we calculated the XRD intensities for given Miller indices using the following formula:[3]

$$I_{hkl} = |S_{hkl}|^2 \cdot M_{hkl} \cdot L$$

$$L = \frac{1 + \cos^4(2\theta_M)\cos^2(2\theta)}{\sin^2\theta \ \cos\theta}$$

Here, M_{hkl} is the multiplicity and L is the Lorentz-polarization factor. The multiplicity was computed as 2^b, where b is the number of non-zero values in the set (*h*, *k*, *l)*. The temperature factor has been neglected in the intensity calculations.

Intensity ratios were determined for various Miller index peaks. A Python script was written to calculate intensity ratios while iterating through occupancy values, x, between 0.5 and 1.0.

The "interp1d" function from the scipy library was employed to estimate the occupancy values of ETO samples based on a series of iteratively-calculated intensity ratios. The "nearest" method of interpolation was used, given the non-linearity of the plotted intensity ratios. Intensity ratio plotting and interpolation was done for the following ratios, obtained from XRD scans: 001:002, 001:004, 001:006, 003:002, 003:004, and 003:006. The average and standard deviation of the occupancy values obtained via interpolation was determined for each sample.

An example of intensity ratio curves obtained through the Python code is shown in **Figures S13**. Six sets of intensity ratios are plotted – 001:00ℓ and 001:00ℓ, where ℓ is 2, 4, or 6. The occupancy of europium in the sample is estimated to be 64.0% ± 0.07 based on interpolation of experimentally-obtained XRD intensity ratios on each of the six curves.
The ordering parameter $\sigma = (N_F - N_E)/N_t$, is defined as the total number of A-site cations N_t, divided by the difference of N_F (number of A-site cations in the nominally filled layer) and N_E (number of A-site cations in the nominally empty layer). The fundamental assumption is that the films are stoichiometric, $EuTa_2O_6$.

The Eu occupancy varies from 1 to 0.5 in nominally filled layer (0.5 to 0 in nominally empty layer) while calculating the intensity ratios between even 00ℓ and odd 00ℓ peaks and was compared to the measured intensity ratios of our samples grown.

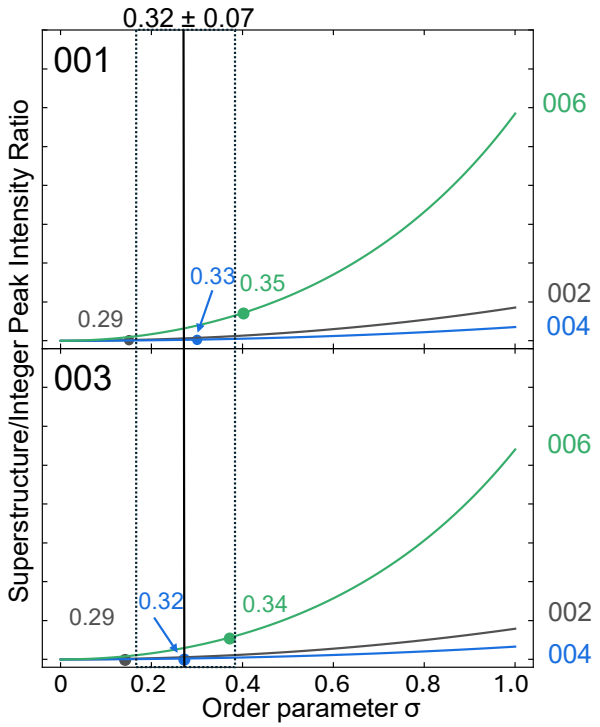

Figure S13: Six curves were created using iterative Python methods. (top) The 001:002, 001:004, and 00 1:006 intensity ratios are plotted; (bottom) The 003:002, 003:004, and 003:006 intensity ratios are plotted. The six black points represent interpolated occupancy values based on the XRD intensity ratios obtained from scans of the sample. All Miller indices are based on the doubled unit cell of ETO.

4. HAADF-STEM electron diffraction

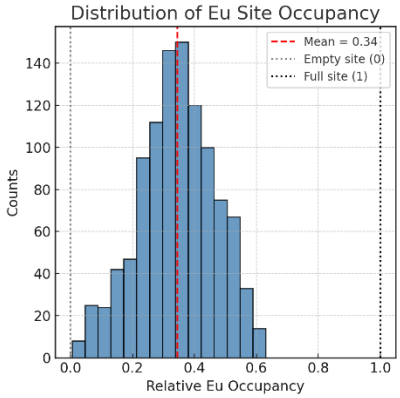

Figure S14: Quantitative HAADF-STEM analysis across 1100 Eu atomic columns for the same 16.3 nm ordered film of $EuTa_2O_6$ thin film grown on $SrTiO_3$ (001).

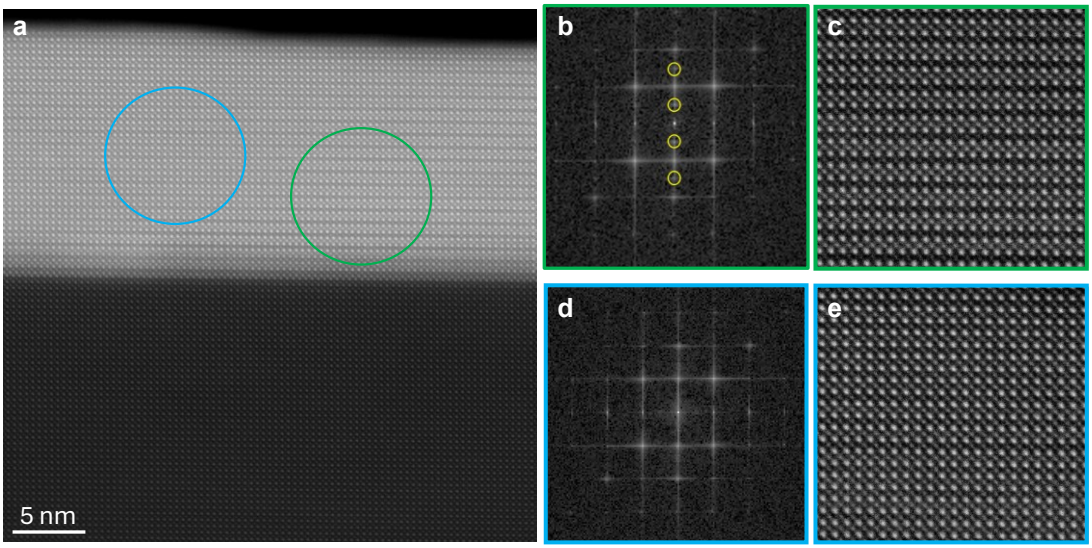

Figure S15: (a) Cross-sectional HAADF-STEM image highlighting regions with differing degrees of europium ordering in a $EuTa_2O_6$ thin film grown on $SrTiO_3$ (001). Two representative regions are marked: one exhibiting clear europium ordering (green circle) and another with reduced ordering (blue circle). (b) Fast Fourier Transform (FFT) from the ordered region (green circle) clearly reveals superlattice reflections (highlighted by yellow circles), confirming out-of-plane europium ordering. (c) Inverse FFT image of the ordered region, emphasizing the periodic arrangement corresponding to the observed superlattice reflections. (d) FFT from the disordered region (blue circle) lacks these superlattice reflections, indicating reduced or absent europium ordering. (e) Inverse FFT image of the disordered region, highlighting the absence of ordering-related periodicity.

5. Additional sample characterization of fractional double perovskite $SrTa_2O_6$

$SrTa_2O_6$ is a fractional double perovskite with a = 3.926 Å and c = 7.940 Å. Similar to $EuTa_2O_6$ the preferred layered hettotype results in an anisotropic bonding (SOJT) arrangement for the octahedrally coordinated Ta^{5+}. Here, the apical Ta-$O_{(z)}$ (Å) bond length towards the vacant layer has shortened to 1.903 Å, while the Ta-$O_{(z)}$ (Å) bond length towards the EuO layer has elongated to 2.066 Å from the symmetrical apical bond distance of 1.980 Å. The SOJT is expected to break the degeneracy of the Ta^{5+} t_{2g}-manifold in a similar fashion as in $EuTa_2O_6$, where the d_{xy} is energetically favored. The d_{xy} orbitals have suppressed out-of-plane hopping and, as a result, the conduction band edge exhibits dispersive behavior along the Γ→X and Γ→M directions while appearing flat along Γ→Z.

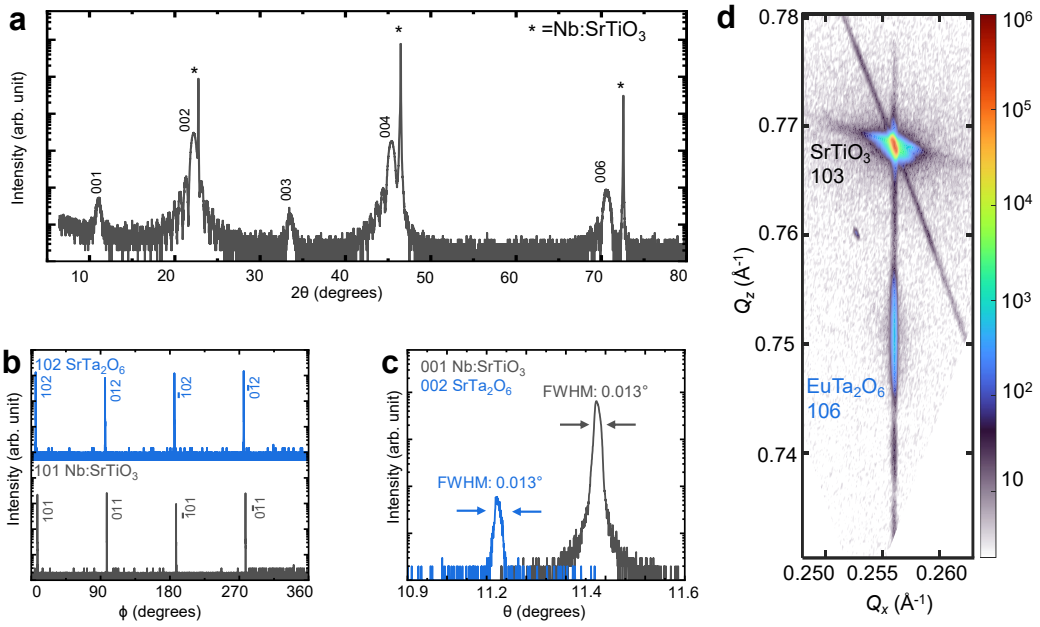

Figure S16: X-ray diffraction of a 14.8 nm thick film of $SrTa_2O_6$ grown on Nb:$SrTiO_3$: **a** Symmetrical θ-2θ scan showing only 00l peaks of $SrTa_2O_6$. Laue oscillations indicate a well-defined film thickness, caused by an abrupt interface between film and substrate. **b** ϕ-scans around the 103-type substrate and 106-type film reflections. d Overlaid rocking curves of 001 $SrTiO_3$ and 002 $SrTa_2O_6$ reflections, showing comparable FWHMs, indicating low out-of-plane mosaicity (Δω ≈ 0.013°). **d** Reciprocal space map (RSM) around the 103 substrate and 106 film reflection. The RSM results confirm that the film is commensurately strained to the substrate.

AFM reveals atomic steps on the as grown films with step heights corresponding to the *c*-axis of the fractional double perovskite. Suggestion step flow growth with a smooth interface between film and substrate. The well-defined surface structure suggests that out-of-plane domains are propagated from the substrate-film to the sample surface. **Figure S17 a** and **b** illustrate the potential surface termination which would result in the observation of step height *d* = 7.4 Å and 3.9 Å.

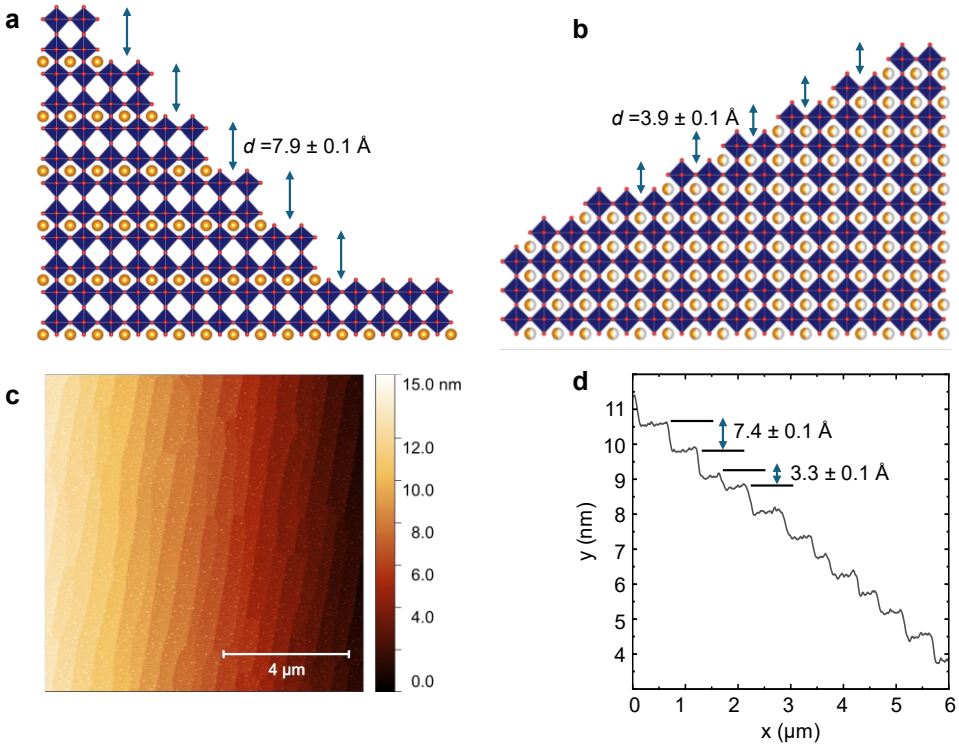

Figure S17: **a** Surface step schematic for $SrTa_2O_6$ with its c-axis perpendicular to the substrate plane. **b** Surface step schematic of $Sr_{0.5}TaO_3$. **c** AFM micrograph of a 14.8 nm thick $SrTa_2O_6$ film on $SrTiO_3$ (001), with a rms of 0.42 nm taking the whole 10 µm area as reference. **d** Extracted line profile (2 µm width) from the same AFM micrograph. Majority of visible step correspond to the elongated unit cell characteristic for the ordered fractional double perovskite.

6. Electronic structure of fractional double perovskite $SrTa_2O_6$

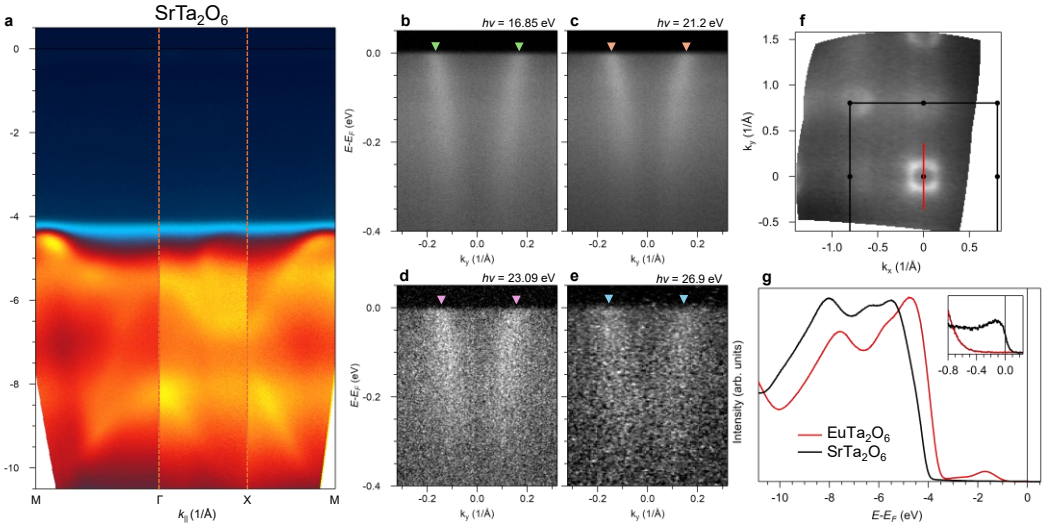

Figure S18: **a** in situ angle-resolved valence band structure of a 14.8nm thick $SrTa_2O_6$ film, measured with an incident photon energy of 21.2 eV. Faint conduction bands crossing E_F are present but extremely weak relative to the O 2p valence bands. **b-e** High-resolution band dispersion of the Ta 5d_{xy} conduction bands crossing E_F, measured at various photon energies corresponding to different plasma gas emission lines. Lines used are Ne-I (16.85 eV), He-Iα (21.2 eV), He-Iβ (23.09 eV), and Ne-II (26.9 eV), spanning 0.46 Å^{-1} in k_z. Ne-I and Ne-II spectra are processed with an algorithm described elsewhere to remove overlapping doublet spectra.[4] The lack of out-of-plane dispersion over this range of k_z indicates the highly 2D character of the Ta 5d_{xy} bands. **f** Corresponding Fermi surface map for He-Iα, integrated over ± 20 meV. Black lines indicate the nominal Brillouin zone boundary for the underlying $SrTiO_3$ substrate. **g** Comparison of angle-integrated valence band spectra of $SrTa_2O_6$ to $EuTa_2O_6$, as duplicated from the main text. The relative shift of O 2p bands to higher binding energies indicates additional electron doping. The inset shows a zoom in on the integrated Fermi edge, indicating increased spectral weight at E_F from the Ta 5d_{xy} conduction bands. All measurements were performed in situ without exposure to atmosphere and with the film held at a temperature of 8 K.

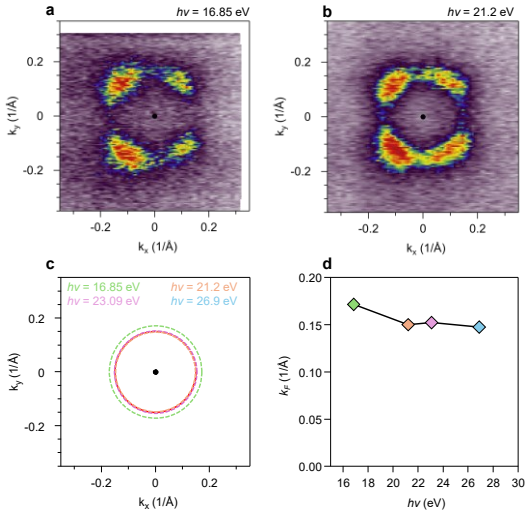

Figure S19: a,b *in situ* angle-resolved Fermi surface maps for a $SrTa_2O_6$ film, measured with Ne-I ($h\nu$ = 16.85 eV, **a**) and He-I ($h\nu$ = 21.2 eV, **b**). Data are integrated about +/- 15 meV of E_F. **c** Projected Fermi surface areas at each photon energy based on measured k_F values from [Figure S18] (panel **d**).

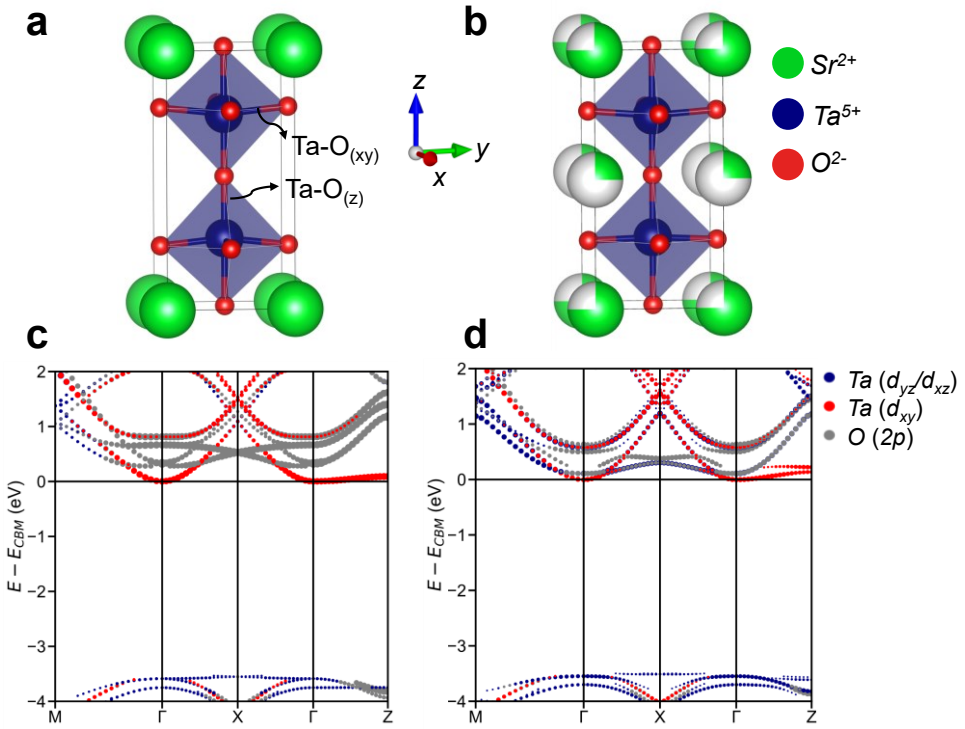

Figure S20: a A-site cation ordering scheme for fully ordered $SrTa_2O_6$. **b** A-site cation ordering scheme for partially ordered $SrTa_2O_6$ where 25 % of the Sr occupies the nominally vacant planes. Illustrations were prepared with VESTA.[5] Orbital-projected band structure of **c** ordered $SrTa_2O_6$ and **d** partially occupied $SrTa_2O_6$ calculated by DFT. Flat bands along Γ→Z persist in partial order.

References:

[1] M. Namba, H. Takatsu, R. Mikita, Y. Sijia, K. Murayama, H.-B. Li, R. Terada, C. Tassel, H. Ubukata, M. Ochi, R. Saez-Puche, E. P. Latasa, N. Ishimatsu, D. Shiga, H. Kumigashira, K. Kinjo, S. Kitagawa, K. Ishida, T. Terashima, K. Fujita, T. Mashiko, K. Yanagisawa, K. Kimoto, H. Kageyama, *J. Am. Chem. Soc.* **2023**, *145*, 21807.

[2] P. J. Brown, A. G. Fox, E. N. Maslen, M. A. O'Keefe, B. T. M. Willis, in *Int. Tables Crystallogr.* (Ed.: E. Prince), International Union Of Crystallography, Chester, England, **2006**, pp. 554–595.

[3] G. S. Rohrer, *Structure and Bonding in Crystalline Materials*, Cambridge University Press, **2001**.

[4] Y. Tarn, M. Sinha, C. Pasco, D. G. Schlom, T. M. McQueen, K. M. Shen, B. D. Faeth, *J. Electron Spectrosc. Relat. Phenom.* **2023**, *265*, 147323.

[5] K. Momma, F. Izumi, *J. Appl. Crystallogr.* **2008**, *41*, 653.